

# Effect of Porosity and Permeability Evolution on Injection-Induced Aseismic Slip

Yuyun Yang<sup>1</sup> and Eric M Dunham<sup>1</sup>

<sup>1</sup>Stanford University

January 20, 2023

## Abstract

It is widely recognized that fluid injection can trigger fault slip. However, the processes by which the fluid-rock interactions facilitate or inhibit slip are poorly understood and some are neglected or oversimplified in most models of injection-induced slip. In this study, we perform a 2D antiplane shear investigation of aseismic slip that occurs in response to fluid injection into a permeable fault governed by rate-and-state friction. We account for pore dilatancy and permeability changes that accompany slip, and quantify how these processes affect pore pressure diffusion, which couples to aseismic slip. The fault response to injection has two phases. In the first phase, slip is negligible and pore pressure closely follows the standard linear diffusion model. Pressurization of the fault eventually triggers aseismic slip in the immediate vicinity of the injection site. In the second phase, the aseismic slip front expands outward and dilatancy causes pore pressure to depart from the linear diffusion model. Aseismic slip front overtakes pore pressure contours, with both subsequently advancing at constant rate along fault. We quantify how prestress, initial state variable, injection rate, and frictional properties affect the migration rate of the aseismic slip front, finding values ranging from less than 50 to 1000 m/day for typical parameters. Additionally, we compare to the case when porosity and permeability evolution are neglected. In this case, the aseismic slip front migration rate and total slip are much higher. Our modeling demonstrates that porosity and permeability evolution, especially dilatancy, fundamentally alters how faults respond to fluid injection.

1           **Effect of Porosity and Permeability Evolution on**  
2                           **Injection-Induced Aseismic Slip**

3                           **Yuyun Yang<sup>1</sup>, Eric M. Dunham<sup>1,2</sup>**

4                           <sup>1</sup>Institute for Computational and Mathematical Engineering, Stanford University

5   <sup>2</sup>Department of Geophysics, Stanford University

6           **Key Points:**

- 7           • Modeling of constant rate fluid injection into a fault predicts steadily propagat-  
8           ing aseismic slip front
- 9           • Migration rate of aseismic slip front increases with injection rate and ranges from  
10           less than 50 to 1000 m/day for typical parameters
- 11           • Dilatancy and permeability enhancement alter system response as compared to  
12           linear pore pressure diffusion

## Abstract

It is widely recognized that fluid injection can trigger fault slip. However, the processes by which the fluid-rock interactions facilitate or inhibit slip are poorly understood and some are neglected or oversimplified in most models of injection-induced slip. In this study, we perform a 2D antiplane shear investigation of aseismic slip that occurs in response to fluid injection into a permeable fault governed by rate-and-state friction. We account for pore dilatancy and permeability changes that accompany slip, and quantify how these processes affect pore pressure diffusion, which couples to aseismic slip. The fault response to injection has two phases. In the first phase, slip is negligible and pore pressure closely follows the standard linear diffusion model. Pressurization of the fault eventually triggers aseismic slip in the immediate vicinity of the injection site. In the second phase, the aseismic slip front expands outward and dilatancy causes pore pressure to depart from the linear diffusion model. Aseismic slip front overtakes pore pressure contours, with both subsequently advancing at constant rate along fault. We quantify how prestress, initial state variable, injection rate, and frictional properties affect the migration rate of the aseismic slip front, finding values ranging from less than 50 to 1000 m/day for typical parameters. Additionally, we compare to the case when porosity and permeability evolution are neglected. In this case, the aseismic slip front migration rate and total slip are much higher. Our modeling demonstrates that porosity and permeability evolution, especially dilatancy, fundamentally alters how faults respond to fluid injection.

## Plain Language Summary

The underground injection of fluids during wastewater disposal, geothermal operations, and other energy-production activities has been linked to the occurrence of earthquakes. In addition to earthquakes, fluid injection can also trigger aseismic slip on faults, that is, frictional sliding that occurs so slowly that seismic waves and ground shaking are not produced. Here we perform computer modeling of fluid injection and aseismic slip, exploring how the injection rate and fluid transport properties influence the aseismic slip response. We speculate that additional complexity in frictional properties and other conditions would cause aseismic slip to be accompanied by numerous, small earthquakes (microseismicity), as is often observed during injection. We quantify the rate at which aseismic slip migrates outward from the injection site and compare predicted migration rates to observed microseismicity patterns. Our model also predicts fluid pressure changes, slip, rock deformation surrounding the fault, and fluid flow paths that might be measurable and used to validate the modeling.

## 1 Introduction

Fluid injection has been associated with the triggering of seismic events in geologically stable regions that previously had minimal detected seismicity (McGarr et al., 2015). Injection is done in the context of wastewater disposal and hydraulic fracturing in oil and gas operations, carbon sequestration, and geothermal energy production (Mazzoldi et al., 2012; Ellsworth, 2013; Ellsworth et al., 2016). Many sequences of small earthquakes have been recorded near injection wells, some of which last for months or years (Horton, 2012; W. Y. Kim, 2013; Wei et al., 2015; Goebel et al., 2016; Eyre et al., 2020). Injection not only triggers microseismic events, but is also capable of triggering damaging earthquakes such as the 2011  $M_w$  5.7 and 2016  $M_w$  5.8 events in Oklahoma (Keranen et al., 2013; Yeck et al., 2017), as well as the 2017  $M_w$  5.4 event in Pohang, South Korea (K. H. Kim et al., 2018). This problem not only impacts the lives of people who face the risk of damaging earthquakes in the affected areas, but also bears important implications for harnessing the Earth’s natural resources safely and responsibly. To effectively assess earthquake hazards, a better understanding of the physical mechanisms underlying fluid-induced seismicity is essential.

63 Several processes have been proposed as the triggering mechanism of injection-induced  
64 seismicity. One of them is pore pressure diffusion (Shapiro et al., 1997; Shapiro & Dinske,  
65 2009), where pressure perturbations expanding out from the injection site reduce the ef-  
66 fective normal stress of the rock matrix, bringing the rock closer to the Coulomb-Mohr  
67 failure criterion (Handin, 1969). Later work has also investigated poroelastic stress changes,  
68 which may dominate over pore pressure at large distances (Segall & Lu, 2015; Chang &  
69 Segall, 2016; Goebel et al., 2017; Goebel & Brodsky, 2018; Szafranski & Duan, 2020),  
70 as the solid matrix at some distance from the injection point initially responds elasti-  
71 cally to fluid injection, promoting critically stressed faults to failure before the arrival  
72 of diffusive pressure perturbations (Deng et al., 2016). Recently, fault loading and re-  
73 activation by aseismic slip has been proposed as another mechanism that is able to trans-  
74 mit elastic stresses far beyond the pressure contours (Guglielmi et al., 2015; Wei et al.,  
75 2015; Bhattacharya & Viesca, 2019; Eyre et al., 2019). Aseismic slip is also thought to  
76 play an important role in the propagation of earthquake swarms, which could be com-  
77 posed of bursts of seismicity with migration velocity consistent with slow slip migration  
78 (Roland & McGuire, 2009; Wei et al., 2015; Shelly et al., 2016; De Barros et al., 2020).  
79 Aseismic slip triggered by fluid injection is the focus of our study.

80 The injection of fluid into a fault not only alters pore pressure and triggers slip,  
81 but also changes properties of the fault zone that in turn impact fluid flow and fault slip  
82 behavior. The most relevant properties here are porosity and permeability. Many exper-  
83 iments, in both the laboratory and in situ, show that dilatancy (the expansion of pores  
84 and the fluids within them) accompanies shear deformation of fault zone rocks (Morrow  
85 & Byerlee, 1989; Rawling et al., 2002; Samuelson et al., 2009; Guglielmi et al., 2015; Cappa  
86 et al., 2018; Proctor et al., 2020; Brantut, 2020). In the absence of fluid flow (i.e., undrained  
87 conditions), dilatancy reduces pore pressure, thus increasing the effective normal stress  
88 and stabilizing the fault (Lockner & Byerlee, 1994; Segall & Rice, 1995; Segall et al., 2010).  
89 Porosity changes also alter permeability. As the pores dilate and more porous space be-  
90 comes connected, permeability is enhanced (Zhu & Wong, 1999; Simpson et al., 2001;  
91 Y. Zhang et al., 2008; Ye & Ghassemi, 2018). This facilitates fluid flow and enables pore  
92 pressure perturbations to reach greater distances along the fault in a shorter period of  
93 time. Pore dilation and permeability enhancement on rough slip surface also depends  
94 on the nature of the surface contacts. Initially mated surfaces exhibit more significant  
95 dilation and permeability enhancement with slip, whereas on unmated surfaces, compaction  
96 and permeability reduction may result from the comminution of surface asperities (Im  
97 et al., 2019). Likewise, experiments involving shearing of fluid-saturated gouge have also  
98 shown both stabilization from dilatancy and destabilization from compaction. It is cer-  
99 tainly evident that the evolution of porosity and permeability, while complex, can fun-  
100 damentally influence fluid flow and fault slip behavior, and therefore needs to be taken  
101 into account in fault models with hydromechanical coupling.

102 Recently, there have been several modeling efforts to characterize the aseismic slip  
103 resulting from fluid injection and how that could potentially affect resulting earthquakes.  
104 Garagash and Germanovich (2012) studied injection into a slip-weakening fault, high-  
105 lighting the key role that prestress (relative to static and dynamic frictional strength)  
106 plays in controlling whether slip is seismic or aseismic. Bhattacharya and Viesca (2019)  
107 modeled quasi-static slip with linear slip-weakening friction, adding step changes in per-  
108 meability in order to fit injection experiment results from Guglielmi et al. (2015). Eyre  
109 et al. (2019) conducted modeling in the context of hydraulic fracturing with rate-and-  
110 state friction and flash heating to show that aseismic slip could progressively load dis-  
111 tal, unstable regions of a fault. Dublanchet (2019) quantified the propagation of aseis-  
112 mic slip on a velocity-strengthening rate-and-state fault, showing how different prestresses,  
113 frictional conditions, hydraulic properties and injection history control the dynamics of  
114 fluid-induced aseismic slip. Wynants-Morel et al. (2020) used 3D hydromechanical mod-  
115 eling on a permeable, slip-weakening fault to characterize slip resulting from different  
116 prestress conditions, and was able to generate features observed in induced earthquake

117 sequences. Laroche et al. (2020) studied how fault prestress, relative to static or dy-  
 118 namic frictional strength, controls whether slip is confined to the fluid-affected zone or  
 119 expands beyond it. Other studies have accounted for the full poroelastic response in ad-  
 120 dition to rate-and-state friction (Pampillón et al., 2018; Torberntsson et al., 2018; Heimis-  
 121 son et al., 2019; Andrés et al., 2019). These, and other, numerical modeling efforts were  
 122 able to explain a wide range of observations in the lab and field, as well as to provide  
 123 insight into various hydromechanical processes. We build on these important studies by  
 124 adopting a more comprehensive modeling approach, incorporating rate-and-state fric-  
 125 tion as well as the evolution of porosity and permeability that accompanies slip and pore  
 126 pressure diffusion, which could have significant effects on the nature of the fault slip.

127 In this study, we investigate the propagation of aseismic slip that is triggered by  
 128 fluid injection. This is done in 2D antiplane shear for a planar, permeable fault in a ho-  
 129 mogeneous elastic solid. The fault is governed by rate-and-state friction with the slip law  
 130 of state evolution. Fluids are confined to the fault, and injection occurs at a specified  
 131 rate into the center of the fault. Porosity and permeability evolve with slip, with per-  
 132 meability related to porosity via a power-law relation. The goal of this study is to eval-  
 133 uate the controlling factors for the initiation and propagation of aseismic slip, and to make  
 134 testable predictions of potentially observable quantities like the migration rate of the aseis-  
 135 mic slip and pore pressure contours, as a function of prestress, frictional parameters, and  
 136 injection rate. Section 2 introduces the governing equations we use for the fault, fluid  
 137 transport, and porosity and permeability evolution. Section 3 lists model parameters and  
 138 displays the simulation results. We showcase comparisons for different prestress condi-  
 139 tions, initial state variables, injection rates, and frictional properties, evaluating their  
 140 relative importance in determining slip behavior. We also highlight how neglecting poros-  
 141 ity and permeability evolution can drastically change the nature of fault slip. Finally,  
 142 in Section 4, we connect our simulations with a limited set of observations and empha-  
 143 size the important role of hydromechanical coupling in characterizing fault response to  
 144 fluid injection.

## 145 2 Governing Equations

### 146 2.1 Fault Model

We consider the 2D antiplane shear problem of a planar fault embedded in a linear  
 elastic medium (Figure 1). The fault has constant total normal stress  $\sigma_n$  and con-  
 stant initial shear stress  $\tau_0$ . The fault is located at  $y = 0$ , and displacements  $u(y, z, t)$   
 (about the prestressed initial state) are in the  $x$ -direction. For computational efficiency,  
 we assume symmetry about the fault, enabling us to model only half the domain ( $y \geq$   
 0). The governing equations for quasi-static antiplane shear deformation of an elastic solid  
 are

$$\frac{\partial \sigma_{xy}}{\partial x} + \frac{\partial \sigma_{xz}}{\partial z} = 0, \quad \sigma_{xy} = \mu \frac{\partial u}{\partial y}, \quad \sigma_{xz} = \mu \frac{\partial u}{\partial z}, \quad (1)$$

where  $\sigma_{xy}$  and  $\sigma_{xz}$  are the quasi-static stress changes associated with displacement  $u$  and  
 $\mu$  is the shear modulus, which we assume is constant. We define slip and slip velocity  
 as

$$\delta(z, t) = 2u(0, z, t) \quad \text{and} \quad V = \frac{\partial \delta}{\partial t}, \quad (2)$$

respectively. The fault boundary conditions are

$$\tau = f(\Psi, V) \bar{\sigma}_n, \quad (3)$$

$$\dot{\Psi} = G(\Psi, V), \quad (4)$$

147 where  $\tau$  is the shear stress and  $\Psi$  is the state variable. Equation (3) sets the shear stress  
 148 equal to the frictional strength, with  $f(\Psi, V)$  being the rate-and-state friction coefficient  
 149 and  $\bar{\sigma}_n = \sigma_n - p$  the effective normal stress calculated as the difference between the  
 150 total normal stress  $\sigma_n$  and pore pressure  $p$ . Equation (4) is the state evolution equation.

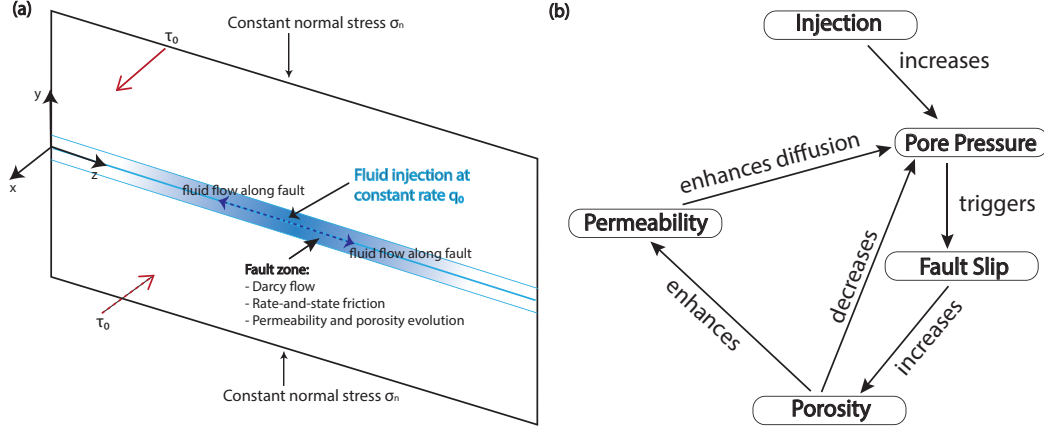


**Figure 1.** (a) The 2D antiplane problem with fluid injection in the middle of the fault and along-fault flow through a permeable fault zone. (b) Feedback relations among pore pressure, fault slip, porosity and permeability.

For the shear stress computation, we switch between the quasi-dynamic approximation with radiation damping (Rice, 1993) at low slip velocities (for which the radiation-damping term is effectively negligible) and a dynamic solver with full inertial effects at high slip velocities (Duru et al., 2019). In the quasi-dynamic approximation,

$$\tau(z, t) = \tau_0 + \sigma_{xy}(0, z, t) - \eta_{rad}V, \quad (5)$$

where  $\tau_0$  is the initial shear stress and  $\eta_{rad}$  is the radiation damping parameter (Rice, 1993). In the dynamic solver, we add the inertial term  $\rho\partial^2u/\partial t^2$ , involving density  $\rho$ , to the momentum balance (1) and disable radiation damping. Switching between quasi-dynamic and fully dynamic solvers is based on the nondimensional ratio  $R = \eta_{rad}V/\tau_{qs}$ , where the numerator is the radiation damping term and the denominator is the quasi-static shear stress (Duru et al., 2019). We choose  $R = 10^{-3}$  to control switching into and out of the fully dynamic solver. For the computation of the rate-and-state friction coefficient, we use the regularized form (Rice et al., 2001):

$$f(\Psi, V) = a \sinh^{-1} \left( \frac{V}{2V_0} \exp\{\Psi/a\} \right) \approx a \ln \left( \frac{V}{V_0} \right) + \Psi, \quad (6)$$

151 where  $a$  is the direct effect parameter and  $V_0$  is the reference velocity. The approximate  
 152 form is valid for  $\tau/(a\bar{\sigma}) \ll 1$ , a condition that is met in all of our simulations. Our choice  
 153 of state variable,  $\Psi$ , is dimensionless and of order unity, making it ideally suited for numerical  
 154 calculations. The change of variable  $\Psi = f_0 + b \ln(V_0\theta/d_c)$ , for state evolution  
 155 distance  $d_c$ , state evolution parameter  $b$ , and state variable  $\theta$  having units of time, brings  
 156 this into the more common form,  $f \approx f_0 + a \ln(V/V_0) + b \ln(V_0\theta/d_c)$ .

We use the slip law (Ruina, 1983) for state evolution, as there is evidence it matches the stress data from large velocity step increases, decreases, and load point holds better than the aging law (Bhattacharya et al., 2017). We have written the slip law in the following form:

$$G(\Psi, V) = -\frac{V}{d_c} [f(\Psi, V) - f_{ss}(V)], \quad (7)$$

where

$$f_{ss}(V) = f_0 + (a - b) \log \left( \frac{V}{V_0} \right) \quad (8)$$

157 is the steady state friction coefficient. This coincides with the usual form of the slip law  
158 when written in terms of  $\theta$ .

Apart from the fault boundary condition, the computational domain has three other boundary conditions:

$$\sigma_{xz}(y, 0, t) = 0, \quad \sigma_{xz}(y, L_z, t) = 0, \quad u(L_y, z, t) = 0, \quad (9)$$

159 where  $L_y$  and  $L_z$  are dimensions of the domain in the  $y$  and  $z$  directions. The bound-  
160 aries perpendicular to the fault are traction-free, and zero-displacement condition on the  
161 remote boundary parallel to the fault indicates that there is no remote plate loading in-  
162 corporated in this model. We use a 50 km  $\times$  50 km domain such that the simulation re-  
163 sults are relatively insensitive to the remote boundaries. Since we are considering a very  
164 short time interval on the scale of days, effects from plate loading can be ignored.

## 165 2.2 Fluid Model

166 Our idealized fluid transport model, like many others in the literature (Walder &  
167 Nur, 1984; Rice, 1992; Wiprut & Zoback, 2000; Saffer & Tobin, 2011; McClure & Horne,  
168 2011; Yamashita, 2013; Bhattacharya & Viesca, 2019; Zhu et al., 2020; Larochelle et al.,  
169 2020), accounts only for along-fault flow. This is motivated by the commonly observed  
170 fault zone structure of a permeable damage zone embedded within relatively imperme-  
171 able host rock (Faulkner & Rutter, 2001; Wibberley, 2002). Fault-normal flow is also lim-  
172 ited by the anisotropic permeability structure of the damage zone, which generally fea-  
173 tures much higher permeability in the fault-parallel direction than in the fault-normal  
174 direction (Faulkner & Rutter, 2001). Nonetheless, the stabilizing effects of dilatancy are  
175 likely to be mitigated, to some extent, by fault-normal flow (Segall & Rice, 1995; Segall  
176 et al., 2010), and arguably the most important extension to our current study would be  
177 to account for this fault-normal flow. Our fluid transport model applies equally well to  
178 the case of smaller faults or fracture systems without well-developed damage zones, in  
179 which fluid flow is restricted to the rough fault interface. The idealization of fracture flow  
180 has been widely used in the porous flow community for studying fractured reservoirs in  
181 otherwise low permeability formations, and has been applied in simulations that couple  
182 with rate-and-state frictional sliding (McClure & Horne, 2011; Norbeck & Horne, 2018).

The continuity of fluid mass, in the absence of fluid sources or sinks, can be expressed as

$$\frac{\partial m}{\partial t} + \frac{\partial(\rho q)}{\partial z} = 0, \quad (10)$$

where  $m$  is the fluid mass per unit volume of rock,  $\rho$  is the fluid density, and  $q$  is the fluid volume flux per unit area of the porous solid (i.e., Darcy velocity). Since  $m = \rho\phi$ , where  $\phi$  is the rock porosity or pore volume fraction, we can write

$$\dot{m} = \rho\dot{\phi} + \phi\dot{\rho} = \rho\dot{\phi} + \phi(\rho\beta_f\dot{p}), \quad (11)$$

183 where  $\beta_f = \rho^{-1}\partial\rho/\partial p$  is the fluid compressibility, and the overdot represents the partial  
184 time derivative (H. F. Wang, 2017).

Inelastic strains during fluid transport and deformation can induce inelastic porosity changes, which influence fluid transport properties (Wong et al., 1997). If the change in porosity is written as the sum of an elastic and a plastic component,  $\dot{\phi} = \phi\beta_\phi\dot{p} + \dot{\phi}_p$  (Walder & Nur, 1984; Segall & Rice, 1995), then

$$\dot{m} = \phi\rho\beta_f\dot{p} + \rho(\phi\beta_\phi\dot{p} + \dot{\phi}_p) = \rho(\phi\beta\dot{p} + \dot{\phi}_p), \quad (12)$$

185 where  $\beta_\phi = \phi^{-1}\partial\phi/\partial p$  is the elastic pore compressibility at fixed normal stress and fixed  
186 fault-parallel strains (Walder & Nur, 1984; Segall & Rice, 1995; Rice, 2006). The com-  
187 bined fluid and elastic pore compressibility is  $\beta = \beta_f + \beta_\phi$ . We have chosen  $\beta_\phi = 0.45$

188 GPa<sup>-1</sup>, which is within the range of foliated gouge compressibility data compiled by Wibberley  
 189 (2002), and  $\beta_f = 0.55 \text{ GPa}^{-1}$ , which is within the range of water compressibility dis-  
 190 cussed in Mase and Smith (1987). Therefore  $\beta = 1 \text{ GPa}^{-1}$ .

Fluid volume flux  $q$  is given by Darcy's law:

$$q = -\frac{k}{\eta} \frac{\partial p}{\partial z}, \quad (13)$$

where  $k$  is the permeability,  $\eta$  is the fluid viscosity, and the effects of gravity are neglected (e.g., as appropriate for flow in the horizontal direction). We rewrite the fluid mass conservation by substituting Equations (12) and (13) into Equation (10) and add a source term for fluid injection:

$$\phi\beta \frac{\partial p}{\partial t} = \frac{\partial}{\partial z} \left( \frac{k}{\eta} \frac{\partial p}{\partial z} \right) - \frac{\partial \phi_p}{\partial t} + q_0 \delta(z), \quad (14)$$

191 where  $q_0$  is a constant injection rate (volume per time per unit distance in the  $x$  direc-  
 192 tion) that is turned on at the start of our simulations ( $t = 0$ ), and  $\delta(z)$  is the Dirac delta  
 193 function that places the source at  $z = 0$ . This is a diffusion equation with hydraulic  
 194 diffusivity  $c = k/(\phi\beta\eta)$ .

195 The evolution of plastic porosity can be viewed as a source/sink term. In the undrained  
 196 case, when compaction occurs,  $\partial\phi_p/\partial t < 0$  and pore pressure increases; when dilation  
 197 occurs,  $\partial\phi_p/\partial t > 0$  and pore pressure decreases.

### 198 2.3 Porosity Model

We adopt the Segall and Rice (1995) formulation of plastic porosity evolution and dilatancy. We recognize that some recent experiments such as Proctor et al. (2020) and Brantut (2020) exhibit more complex behaviors that cannot be captured by this formulation. However, as this remains the most widely used model for dilatancy within the earthquake modeling community, we believe it is the logical choice for a first step to incorporate porosity evolution in a fully coupled fluid-fault model. The formulation reads:

$$\frac{\partial \phi_p}{\partial t} = -\frac{V}{d_c} (\phi_p - \phi_{p,ss}(V)), \quad (15)$$

where the steady-state plastic porosity is

$$\phi_{p,ss}(V) = \phi_{p,0} + \epsilon \ln \frac{V}{V_0}, \quad (16)$$

199 where  $\phi_{p,0}$  is the steady-state plastic porosity at reference velocity  $V_0$  and  $\epsilon$  is a dilatancy  
 200 coefficient, which experiments suggest is on the order of  $10^{-4}$  (Segall & Rice, 1995).

The elastic component of porosity  $\phi_e$  evolves according to the definition stated earlier:

$$\frac{\partial \phi_e}{\partial t} = \phi\beta_\phi \frac{\partial p}{\partial t}. \quad (17)$$

### 201 2.4 Permeability Model

Permeability evolution is intrinsically linked to the evolution of porous space. As pore connections are enhanced by dilation or the removal of fines along pore throats, permeability (and storage) are enhanced (Bernab et al., 2003). There is no one-to-one relationship between permeability and porosity applicable to all porous media, as the relation is very much dictated by the specific operating process, material, and microscopic pore structure. Nonetheless, a widely accepted permeability-porosity relationship is the generalized power law (Walder & Nur, 1984; Nelson, 1994; Zhu et al., 1995; Civan, 2001;

Luquot & Gouze, 2009; Menke et al., 2015; L. Zhang et al., 2015):

$$\frac{k}{k_0} = \left( \frac{\phi}{\phi_0} \right)^\alpha, \quad (18)$$

where  $k_0$  and  $\phi_0$  are the reference permeability and porosity, and the exponent  $\alpha$  has a wide range of values from 1 to 25, depending on the rock type and confining stress level. David et al. (1994), Bernab et al. (2003), and Johannes et al. (2018) have compiled some published data on the values of  $\alpha$  for different materials and processes. Even for the same rock type and process, the value of  $\alpha$  is far from unique. We have chosen  $\alpha = 20$ , at the higher end of observed values, but one that is consistent with experiments on certain types of sandstones (David et al., 1994). Lower values of  $\alpha$  would result in less enhancement in permeability and fluid flow in response to porosity changes, while retaining the same dilatancy-induced suction.

For the reference  $k_0$ , we have chosen  $10^{-12} \text{ m}^2$ , consistent with some recent in situ experiments (Guglielmi et al., 2015; Bhattacharya & Viesca, 2019; Laroche et al., 2020), but perhaps on the higher end of fault zone permeability in basement rocks (Y. Zhang et al., 2013). The reference porosity  $\phi_0$  is chosen to be 10%, which is representative of fault gouges (Segall & Rice, 1995), and we have split this porosity equally into an elastic component and a plastic component for the purpose of modeling porosity separately in two ways.

### 3 Numerical Simulations

We have conducted a wide range of simulations to explore the effects of different initial state and prestress conditions, fluid injection rates, and frictional properties. We use a high-order SBP-SAT finite difference method for spatial discretization along with adaptive time stepping, with error control on slip and the state variable (Erickson & Dunham, 2014; Allison & Dunham, 2018; Duru et al., 2019). Pressure (14) and elastic porosity (17) are solved implicitly using backward Euler (using operator-splitting at the Runge-Kutta stage level), while slip (2), state variable (4), and plastic porosity (15) are solved explicitly an adaptive Runge-Kutta method (Zhu et al., 2020).

In the following sections, we have chosen to focus primarily on velocity-strengthening faults, as under upper crustal conditions and for temperatures less than  $120^\circ\text{C}$ , laboratory experiments have shown that gouges for characteristic lithologies associated with injection-induced seismicity (e.g., carbonates, shales, and organic-rich reservoir rocks) show predominantly velocity-strengthening behavior (Kohli & Zoback, 2013; Scuderi et al., 2017). Available data and studies also show that less than 2% of injection wells across the United States have been associated with induced earthquakes (Yehya et al., 2018), and evidence from some field sites suggests that a significant fraction of the induced slip and deformation is aseismic (Cornet et al., 1997; Evans et al., 2005; Zoback et al., 2012; Guglielmi et al., 2015; Duboeuf et al., 2017; Villiger et al., 2020). Results for velocity-weakening faults are presented at the end of Section 3.

Below, we list the parameters used in the simulations and explore the results systematically.

#### 3.1 Parameters

The simulations use grid stretching in both the  $y$  and  $z$  directions, with finer grids near the injection site and sparser grids farther from there. The grid spacing within 2.5 km of the injection site is constant at 0.67 m, and farther from there stretches out according to a hyperbolic sine function. A critical length scale characterizing the process zone at the tip of a propagating rupture is  $L_b = \mu d_c / \bar{\sigma}_n b$  (Dieterich, 1992; Ampuero & Rubin, 2008), at least for the aging state evolution law, with comparatively less known

247 for the slip law (Viesca, 2020).  $L_b$  is about 60 m in our set-up. Therefore, it is resolved  
 248 by approximately 100 grid points near the injection site where the slip front initiates,  
 249 and provides adequate resolution for the simulations. The parameters in Table 1 are the  
 250 same across simulations except for the ones indicated as variable.

Symbol	Description	Value
$L_y$	Domain size in $y$ direction	50 km
$L_z$	Domain size in $z$ direction	50 km
$\mu$	Shear modulus	32.4 GPa
$d_c$	Characteristic state evolution distance	1 mm
$a$	Rate-and-state direct effect parameter	0.01
$b$	Rate-and-state state evolution parameter	variable
$\tau_0$	Initial shear stress	variable
$\Psi_0$	Initial state variable	variable
$q_0$	Fluid injection rate	variable
$\sigma_n$	Normal stress	50 MPa
$V_0$	Reference velocity	$10^{-6}$ m/s
$f_0$	Reference friction coefficient	0.6
$\phi_{e,0}$	Reference elastic porosity	0.05
$\phi_{p,0}$	Reference plastic porosity	0.05
$k_0$	Reference permeability	$10^{-12}$ m <sup>2</sup>
$\alpha$	Coefficient for porosity-permeability relation	20
$\epsilon$	Dilatancy coefficient	$2 \times 10^{-4}$
$\beta_f$	Fluid compressibility	$0.55 \text{ GPa}^{-1}$
$\beta_\phi$	Elastic pore compressibility	$0.45 \text{ GPa}^{-1}$
$\eta$	Fluid viscosity	$10^{-3}$ Pa s

**Table 1.** Reference parameters

### 251 3.2 Initial Conditions

252 We set a uniform prestress  $\tau_0$  and a uniform state variable  $\Psi_0$  across the entire fault  
 253 at  $t = 0$ . From these conditions, and the fact that stress changes from slip are zero, we  
 254 determine the initial slip velocity on the fault by equating shear stress and frictional strength  
 255 (3), and computing slip velocity using bracketed Newton’s method (Kozdon et al., 2013).

256 We set the initial elastic porosity  $\phi_{e,init} = 0.05$ , but the initial plastic porosity  
 257 is different depending on the initial slip velocity. For simplicity, we set the initial plas-  
 258 tic porosity,  $\phi_{p,init}$ , to its steady state value at the initial slip velocity using (16) to com-  
 259 pute the initial plastic porosity  $\phi_{p,init}$ . This value, added to the initial elastic porosity,  
 260 gives the total initial porosity  $\phi_{init} = \phi_{e,init} + \phi_{p,init}$ .

261 The initial permeability is computed as  $k_{init} = k_0(\phi_{init}/\phi_0)^\alpha$ , where  $\phi_0 = \phi_{e,0} +$   
 262  $\phi_{p,0}$  is the reference total porosity, which is 0.1 here.

263 The higher  $\tau_0$  is, the higher the initial slip velocity, resulting in higher initial poros-  
 264 ity and permeability. The opposite occurs for higher initial state  $\Psi_0$ . This is a result of  
 265 the direct effect from rate-and-state friction. Figure 2 shows the relationship among these  
 266 variables.

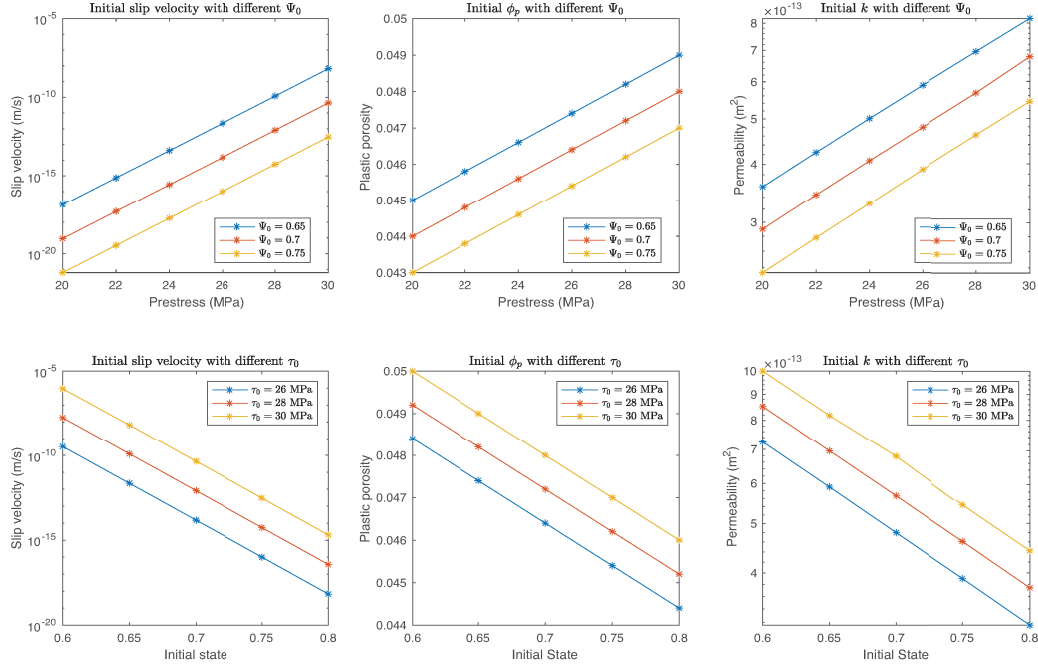


**Figure 3.** Fault response to fluid injection in the velocity-strengthening reference case. Space-

time plots of (a) slip velocity with pressure contours, (b) slip, (c) shear stress, (d) friction coefficient. There are two phases in the fault response to injection: an initial activation period with effectively linear diffusive pressurization, increasing friction coefficient, and negligible slip; followed by a second phase with constant-rate migration of aseismic slip that is driven by elastic stress transfer. Dilatant suction occurs at the slip front and causes pressure contours to propagate at constant rate during this second phase.

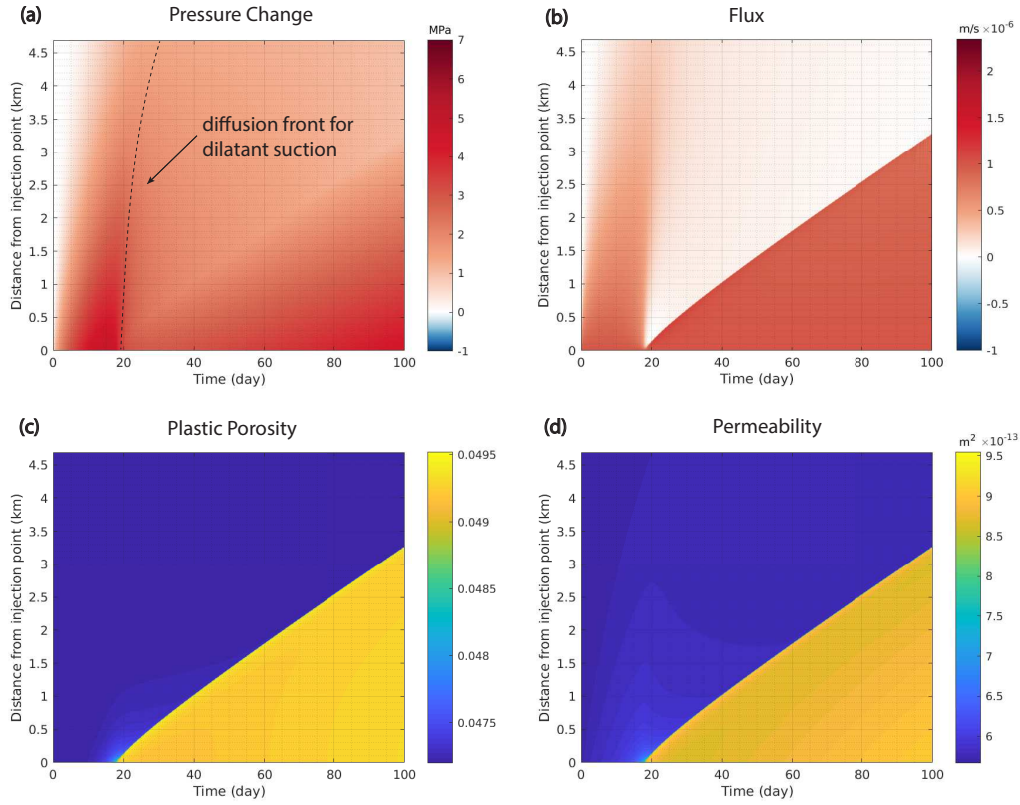


**Figure 4.** Fault response to fluid injection in the velocity-strengthening reference case. Space-time plots of (a) pressure change, (b) fluid flux, (c) plastic porosity, (d) permeability.

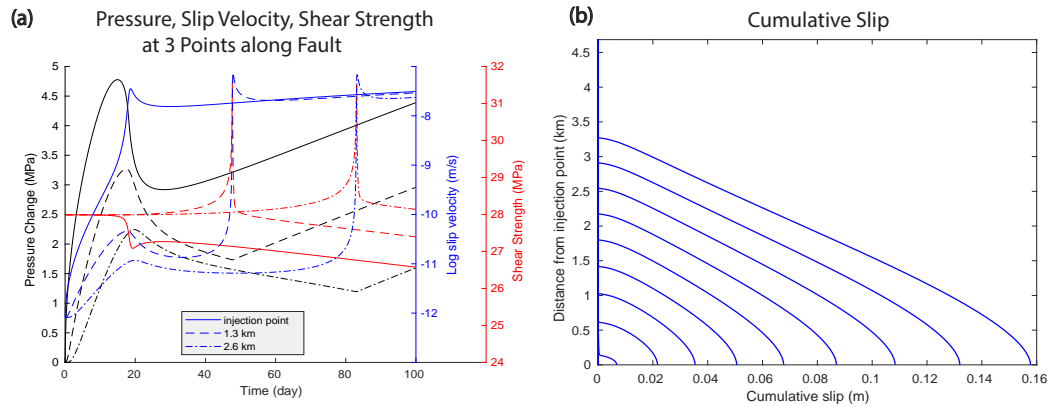


**Figure 5.** Fault response to fluid injection in the velocity-strengthening reference case. (a) Time series plot of pressure change (black), slip velocity (blue), and shear stress (red) at three points along the fault:  $z = 0, 1.3 \text{ km},$  and  $2.6 \text{ km}$ . (b) Cumulative slip plotted at 10-day intervals.

279  
280

Figures 3 and 4 show the fault response to fluid injection. There are two phases to this response. The first phase is an activation period with negligible slip, during which

281 the pore pressure evolution is well approximated by a linear diffusion model (since di-  
 282 latancy and changes in storage and permeability are negligible). Pressure at the injec-  
 283 tion site increases as the square-root of time, decreasing effective normal stress. Friction  
 284 coefficient increases in response to the rate-and-state direct effect as effective normal stress  
 285 decreases. During this phase, there is almost no change in shear stress, porosity, and per-  
 286 meability as slip and slip velocity are very small. The second phase is marked by the on-  
 287 set of significant crack expansion, where the aseismic slip front starts to propagate out-  
 288 ward at constant rate. During this phase, significant dilatancy and a drop in pore pres-  
 289 sure occur at the slip front. Pressure contours deviate from the linear diffusion model,  
 290 due to dilatancy and other nonlinearities, and begin to propagate at a constant rate, al-  
 291 though more slowly than the aseismic slip front. Also note that during the duration of  
 292 the simulation, aseismic slip lags behind the commonly used  $z = \sqrt{4\pi ct}$  prediction from  
 293 linear pore pressure diffusion, where  $c$  is the hydraulic diffusivity (Shapiro et al., 1997;  
 294 Shapiro & Dinske, 2009). However, the pore pressure contours in our model no longer  
 295 follows linear diffusion due to the two-way coupling between fluid flow and fault slip.

296 We now discuss in more detail the first phase of the response to injection. The ini-  
 297 tial localized slip rate acceleration can be understood as a balance between the rate-and-  
 298 state direct effect and the rate of change of effective normal stress near the injection site  
 299 (Dublanche, 2019). As the slip velocity is low ( $< 10^{-9}$  m/s), dilatancy is negligible and  
 300 changes in permeability and storage from the pressure-dependence of elastic porosity are  
 301 also extremely small. Therefore, pore pressure diffusion (Figure 4a) is effectively linear.  
 302 This is also evidenced by the 0.5 MPa and 2.5 MPa pressure contours in Figure 3a be-  
 303 fore 20 days, which advance in proportion to the square-root of time. Because slip is neg-  
 304 ligible in this first phase (Figure 3b), the shear stress remains effectively constant (Fig-  
 305 ure 3c). The direct effect causes the friction coefficient to increase as effective normal  
 306 stress decreases at fixed shear stress (Figure 3d). This increases slip velocity to values  
 307 between  $10^{-8}$  and  $10^{-7}$  m/s (Figure 3a). When slip becomes comparable to the state  
 308 evolution distance (Figure 3b), friction begins to evolve toward a lower, steady state value.  
 309 This frictional weakening leads to a stress drop that builds a stress concentration just  
 310 outside a slipping patch around the injection site, initiating an outwardly propagating  
 311 slip front about 20 days after the injection starts.

312 Now consider the second phase of the response, in which aseismic slip initiates near  
 313 the injection site and migrates along the fault at a constant migration rate of about 35  
 314 m/day. At the start of this phase, around the injection site, slip velocity increases to about  
 315  $10^{-7}$  m/s, increasing plastic porosity. This increases permeability (and, to a lesser ex-  
 316 tent, storage) but causes dilatant strengthening by reducing pore pressure (Figure 4c,d).  
 317 However, permeability is only increased by about 50%. Even though this enhances fluid  
 318 flow and pressure diffusion along the fault, the effect is secondary as compared to dila-  
 319 tant strengthening. At the onset of significant slip around 20 days, dilatancy near the  
 320 injection site causes a substantial reduction in pressure as the fluid expands into newly  
 321 dilated pore space. This suction near the injection site triggers a diffusive pressure re-  
 322 duction response that expands outward along the fault (Figure 4a), reducing fluid flux  
 323 to nearly zero (Figure 4b). We have drawn a  $z = \sqrt{4\pi ct}$  contour in Figure 4a to mark  
 324 the diffusive response to dilatant suction, which advances across the fault in a few days,  
 325 consistent with the predicted hydraulic diffusion time. Away from the injection site, pres-  
 326 sure continues to decrease gradually and other conditions on the fault remain relatively  
 327 constant until the arrival of the slip front.

328 Dilatancy at the slip front reduces pressure (Figure 4a) and suppresses further ac-  
 329 celeration of the slip front, despite mild enhancement of permeability. Pressure diffusion  
 330 in this second phase departs substantially from linear pore pressure diffusion due to di-  
 331 latancy and the two-way coupling between slip and pressure changes. Pore pressure con-  
 332 tours in this phase migrate at a constant rate that is slower than the migration rate of  
 333 the aseismic slip front. We also note that fluid flux increases abruptly from nearly zero

at the slip front to a relatively constant value within the slipping part of the fault behind the slip front (Figure 4b).

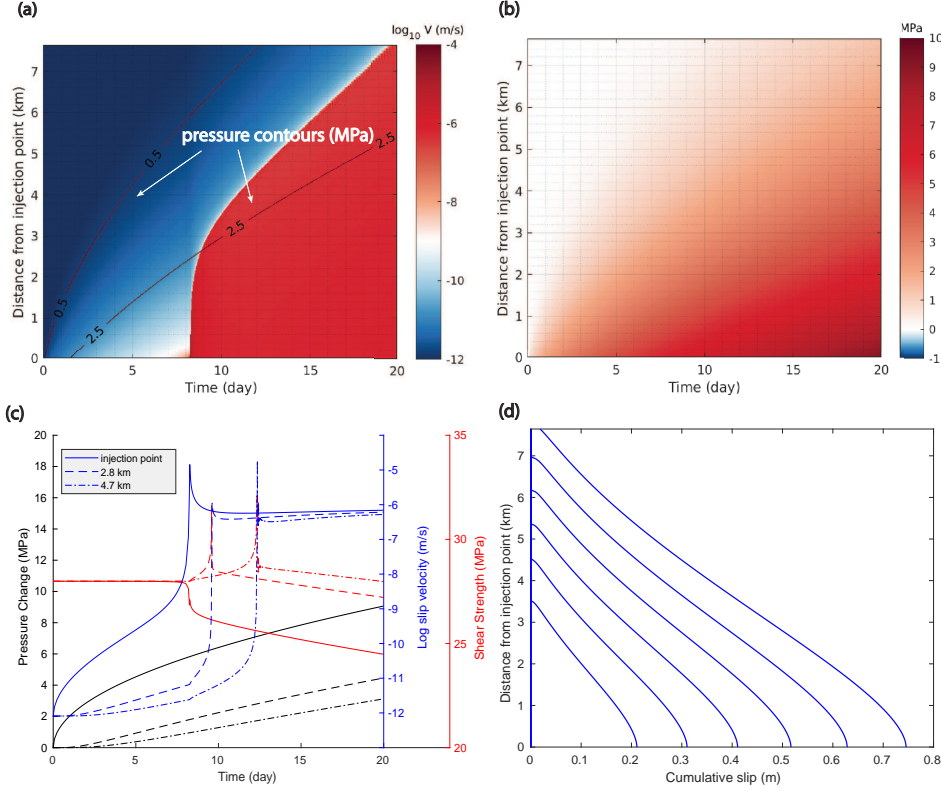
A central question here is, what drives the aseismic slip front? We first note the shear stress concentration at the slip front (Figure 3c), similar to that at the tip of a shear crack. The friction coefficient decreases with state evolution toward a relatively constant value behind the slip front, leading to stress drop and slip behind the slip front. Continued injection leads to additional pressurization of the slipping portion of the fault, at relatively constant friction coefficient, causing additional stress drop and slip. We speculate that elastic stress transfer from slip in this central region provides the loading that drives the aseismic slip front.

Figure 5a provides an alternative view of these effects by showing time series of pressure, slip velocity, and shear stress at three locations along the fault. At all locations, pressure initially rises as the square-root of time during the first phase, consistent with the linear diffusion model prediction, before dropping during the diffusive response to dilatancy near the injection site at the start of the second phase. Then the slip front begins to propagate outward. Pressure reaches a minimum value at the slip front, and then begins to increase at an almost constant rate with the onset of slip and fluid flux. This repressurization, and gradual drop in shear stress, occurs because the fluid delivered by the sustained injection cannot be fully accommodated by the dilated pore space. All of these features, taken together, suggests that injection pressurizes the fault interior, causing stress drop and slip, which through elastic stress transfer maintains the stress concentration at the migrating slip front.

Figure 5b shows the cumulative slip over 100 days along the fault, with each successive line spaced 10 days apart. The largest slip occurs at the injection point. Over 100 days, the center of the fault has accumulated 0.16 m of slip, which translates to an average slip velocity of about  $2 \times 10^{-8}$  m/s. This large amount of slip, if occurring on a sufficiently shallow fault, should be detectable with geodetic observations as well as deformation or even shear failure of the casing in wells that cross the fault.

### 3.4 No Porosity or Permeability Evolution (One-Way Coupling)

Having presented and explained the solution from our fully coupled model that accounts for porosity and permeability evolution, we now discuss how ignoring porosity and permeability evolution impacts the nature of the solution. In this section, we consider the slip response to linear pore pressure diffusion, with one-way coupling from pore pressure changes to fault slip through changes in effective stress and shear strength. This one-way coupling approach has been widely used in recent studies (Bhattacharya & Viesca, 2019; Dublanche, 2019). In fact, the simulation set-up in this section is identical to that in Dublanche (2019), except for our use of the slip law instead of the aging law for state evolution. Results are summarized in Figure 6. As in our previous model, there are two phases of the fault response to injection. The first phase has negligible slip and shear stress change, with accelerating slip velocity near the injection site bringing the fault toward instability. The second phase features the outward migration of an aseismic slip front. Consistent with Dublanche (2019), the slip front advances beyond the (linear diffusion) pressure contours. Despite these general similarities with our previous simulations, there are substantial quantitative differences. First, outward slip migration is triggered much earlier, at about 8 days as compared to 20 days in the previous case. The peak slip velocity at the slip front is very high ( $\sim 10^{-4}$  m/s, about two orders of magnitude higher than in our previous model with dilatancy). Moreover, the migration rate is 400 m/day, over ten times higher than in our previous model. All of these difference contribute to much larger slip; slip at the injection point reaches almost 0.9 m after just 20 days. Therefore, we conclude that the dilatant strengthening effect is very significant and drastically changes the nature of the resulting slip.



**Figure 6.** Fault response to fluid injection in the velocity-strengthening reference case, but neglecting porosity and permeability evolution. Space-time plots of (a) slip velocity and (b) pressure change. (c) Time series of pressure change (black), slip velocity (blue), and shear stress (red) at three points along the fault:  $z = 0, 2.8 \text{ km}$ , and  $4.7 \text{ km}$ . (d) Cumulative slip plotted at 2-day intervals. Slip is much larger, is triggered earlier, and migrates at a much faster rate than in the model accounting for porosity and permeability evolution (Figures 3–5).

385

### 3.5 Effect of Prestress

In this and the following sections we return to models accounting for porosity and permeability evolution, but vary several model parameters to explore controls on the fault response. Here, we vary the prestress  $\tau_0$ . We discuss results in terms of the closeness-to-failure ratio:

$$CTF = \frac{\tau_0}{f_0(\sigma_0 - p_0)}. \quad (19)$$

386

387

388

389

390

391

The closer  $CTF$  is to unity, the closer the fault is to failure. This ratio plays a central role in the fluid injection studies of Bhattacharya and Viesca (2019) and Wynants-Morel et al. (2020). Moreover,  $CTF$  is a useful means of quantifying the pressure perturbation that is required to initiate slip on a fault obeying a Mohr-Coulomb failure criterion (Norbeck & Horne, 2018). Figure 7 shows results for  $\tau_0 = 26, 28$ , and  $30 \text{ MPa}$ , which correspond to  $CTF = 0.867, 0.933$ , and  $1$ .

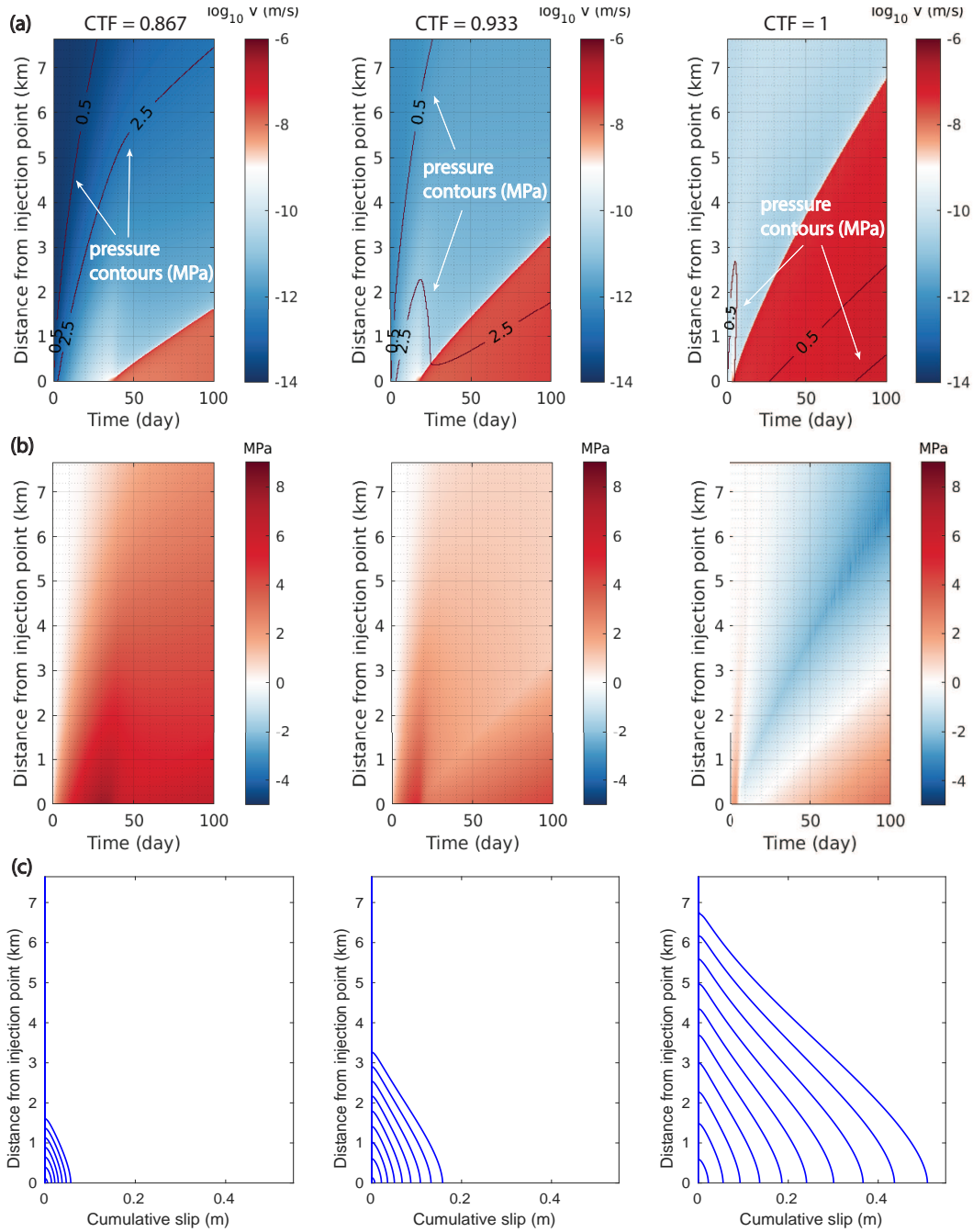


**Figure 7.** Space-time plots of (a) slip velocity and (b) pressure change, and (c) cumulative slip at 10-day intervals, for  $CTF = 0.867, 0.933,$  and  $1$  from left to right. Higher  $CTF$  leads to faster migration rates of the aseismic slip front, despite stronger dilatancy. Cumulative slip also increases with  $CTF$ .

392 Our reference case discussed in Section 3.3 is the middle panel in Figure 7. On the  
 393 left and right are cases with lower and higher prestress, respectively. First, the closer the  
 394 fault is to failure, the earlier significant aseismic slip is triggered. With  $CTF = 0.867$ ,  
 395 aseismic slip with velocity greater than  $10^{-9}$  m/s is only triggered at around 40 days,  
 396 whereas for  $CTF = 0.933$ , it is triggered at 20 days, and for  $CTF = 1$ , 5 days. Sec-

397 ond, the slip front migration rate increases with increasing  $\tau_0$ . This is not surprising given  
 398 that higher  $\tau_0$  means higher  $CTF$  and also larger stress drop, providing more strain en-  
 399 ergy to drive the expanding slip front. Even though dilatancy is greater for a higher  $\tau_0$ ,  
 400 it is does not counteract the additional stress drop. Delayed triggering and lower slip rate  
 401 for lower prestress conditions is also observed in experimental studies such as Scuderi  
 402 et al. (2017).

403 It is also notable that pressure diffusion in the beginning is a lot faster than slip  
 404 front propagation for lower  $\tau_0$ , as dilatancy is weaker. The difference is quite pronounced  
 405 across the cases examined here when we look at the 0.5 MPa and 2.5 MPa contours in  
 406 Figure 7a. Going to higher  $\tau_0$ , the aseismic slip front outpaces the pore pressure contours  
 407 much sooner and their gap becomes much wider. In Figure 7b we can see that the pres-  
 408 sure change even becomes negative for  $CTF = 1$  due to the high slip velocity creat-  
 409 ing very strong dilatant suctions. Therefore, taking dilatancy into account with our cur-  
 410 rent formulation has two implications. First, there is an initial period of time over which  
 411 dilatancy has not had a significant impact yet and the slip front lags behind the pres-  
 412 sure contours. Second, in faults closer to failure, the aseismic slip front overtakes the pore  
 413 pressure diffusion earlier.

414 Finally, Figure 7c shows the cumulative slip. Increasing  $CTF$  makes a large dif-  
 415 ference in the total slip. Therefore, understanding the prestress condition of a fault be-  
 416 fore injection has important implications on the potential amount of slip that can be trig-  
 417 gered.

### 418 **3.6 Effect of Initial State**

419 Next we consider the influence of the initial state variable  $\Psi_0$ . With other initial  
 420 conditions and parameters fixed, higher  $\Psi_0$  results in a lower initial velocity (Figure 2).  
 421 Therefore we anticipate that the trend here would be the opposite of that discussed in  
 422 the previous section, and indeed, we see in Figure 8 that increasing  $\Psi_0$  results in aseis-  
 423 mic slip being triggered at later times and slower slip front migration rates. In all three  
 424 cases, the maximum slip velocity reached is about the same, therefore the dilatancy ef-  
 425 fect approximately the same, in contrast to the large differences seen when we alter the  
 426 prestress. The total slip increases for lower  $\Psi_0$ .

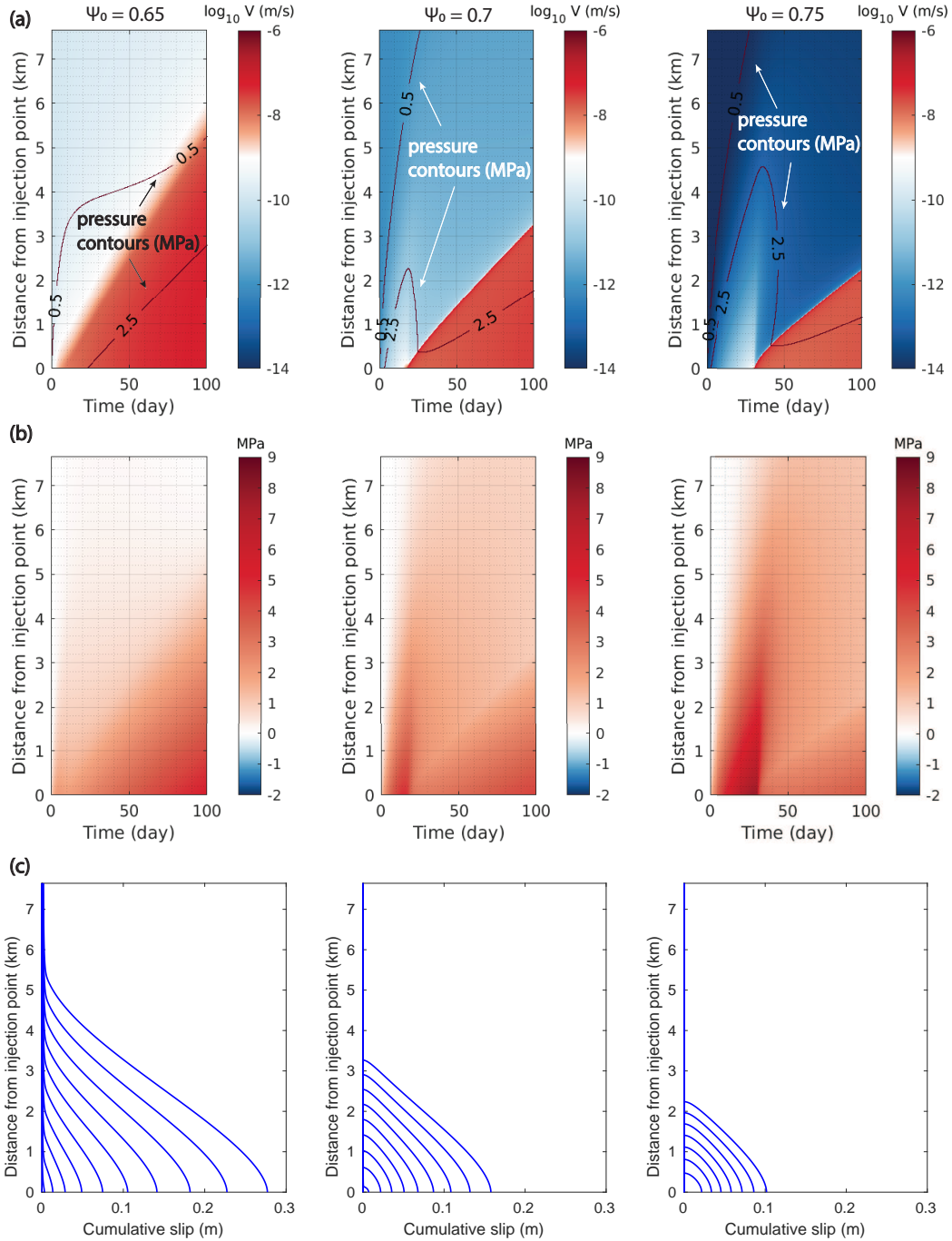


**Figure 8.** Space-time plot of (a) slip velocity and (b) pressure change, and (c) cumulative slip at 10-day intervals, for  $\Psi_0 = 0.65, 0.7, 0.75$  from left to right. The higher  $\Psi_0$  is, the slower the aseismic slip front propagation.

### 3.7 Effect of Injection Rate

We now examine the effect of the injection rate. Figure 9 shows the slip velocity and pressure change for  $q_0 = 10^{-6}, 2 \times 10^{-6},$  and  $4 \times 10^{-6}$  m/s. Higher injection rates trigger slip earlier. Slip velocity is also higher and the slip front propagates faster. Even though dilatancy is stronger for higher injection rates, the elastic stress transfer due to

427

428

429

430

431

432 larger stress drop as a result of higher pore pressure perturbations is the dominant ef-  
433 fect. The slip front takes less time to outpace the pore pressure contours for higher in-  
434 jection rates. Furthermore, as the injection rate doubles, the total amount of slip grows  
435 significantly. With  $q_0 = 10^{-6}$  m/s, the slip over 100 days is less than 3 cm, but it grows  
436 to close to 20 cm for  $q_0 = 2 \times 10^{-6}$  m/s and 80 cm for  $q_0 = 4 \times 10^{-6}$  m/s. However,  
437 when we consider the same total injected volume, the amount of slip is in fact not that  
438 different across the different injection rates. The slip over 100 days for  $q_0 = 10^{-6}$  m/s  
439 is slightly lower than the slip over 50 days for  $q_0 = 2 \times 10^{-6}$  m/s, which is about the  
440 same as the slip over 25 days for  $q_0 = 4 \times 10^{-6}$  m/s. These are marked in red in Fig-  
441 ure 9c. Nevertheless, as higher injection rate is able to trigger significant amounts of slip  
442 earlier, in actual injection operations, it is a major risk factor to control. Similar con-  
443 clusions regarding the importance of pressurization rate have also been reached in some  
444 experimental (L. Wang et al., 2020) and modeling (Alghannam & Juanes, 2020) stud-  
445 ies.

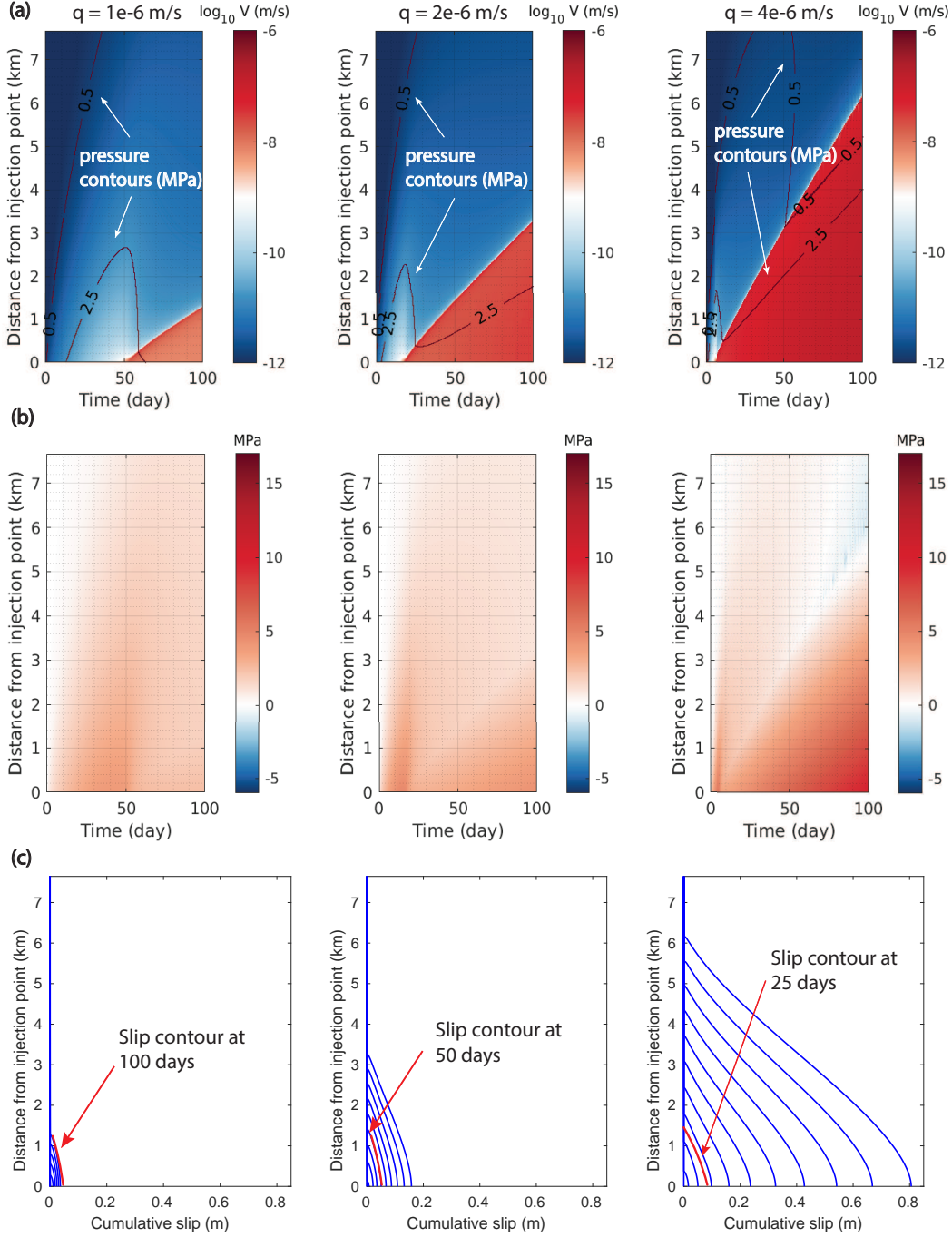


**Figure 9.** Space-time plots of (a) slip velocity and (b) pressure change, and (c) cumulative slip at 10-day intervals, for different injection rates  $q_0 = 10^{-6}$ ,  $2 \times 10^{-6}$  and  $4 \times 10^{-6}$  m/s. The higher the injection rate, the higher the slip velocity, and the faster the aseismic slip front propagates. Total slip also increases dramatically if one considers the same injection time. Red slip contours in (c) indicate times when the total injected volume is identical across all simulations, highlighting that the total slip for the same injected volume is similar.

446

In Figure 10, we quantify migration rates of the aseismic slip front and the 2.5 MPa pore pressure contour as a function of injection rate  $q_0$ . In fact, we see that for higher

447

448 injection rates, the 0.5 MPa contour also comes down due to stronger dilatancy effect  
 449 and travels at the same speed as the 2.5 MPa contour. The migration rate is measured  
 450 as the steady state value that is reached and sustained at later times. Fitting the curves  
 451 to a power-law function of  $q_0$  shows a close match. The fitting functions are  $1.725 \times 10^6 q_0^{0.8139}$   
 452 for the aseismic slip front and  $1.8 \times 10^6 q_0^{0.864}$  for the pore pressure contours (for mi-  
 453 gration rate and  $q_0$  in m/day).

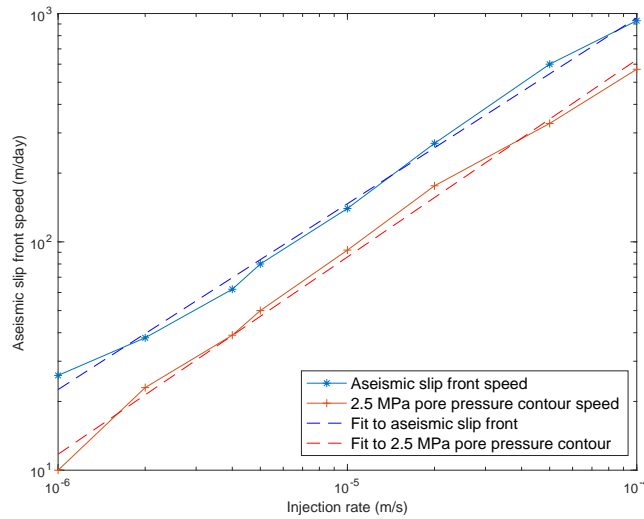


**Figure 10.** Steady state migration rates of aseismic slip front (blue) and 2.5 MPa pore pressure contour (red) for different injection rates  $q_0$ . Power-law fits are plotted in dotted lines.

454

### 3.8 Effect of Frictional Properties

455 Finally, we examine the influence of frictional properties. In Figure 11, we show  
 456 the comparison plots for  $a-b = 0.001, 0.005$  and  $0.01$  with  $a = 0.01$  held fixed. Over-  
 457 all, the changes in aseismic slip front migration rate and the total amount of slip from  
 458 varying  $a-b$  are much smaller than when other model parameters are varied, although  
 459 there are some subtle differences. The differences arise from differences in residual fric-  
 460 tion behind the slip front, which decreases as  $a-b$  increases (because slip velocities are  
 461 less than the reference velocity  $V_0$  at which steady state friction equals  $f_0$ ). This causes  
 462 slip to initiate slightly earlier and leads to somewhat faster migration rates of the slip  
 463 front for larger  $a-b$ . Figure 12 shows more details of the time evolution of friction co-  
 464 efficient at the injection point.

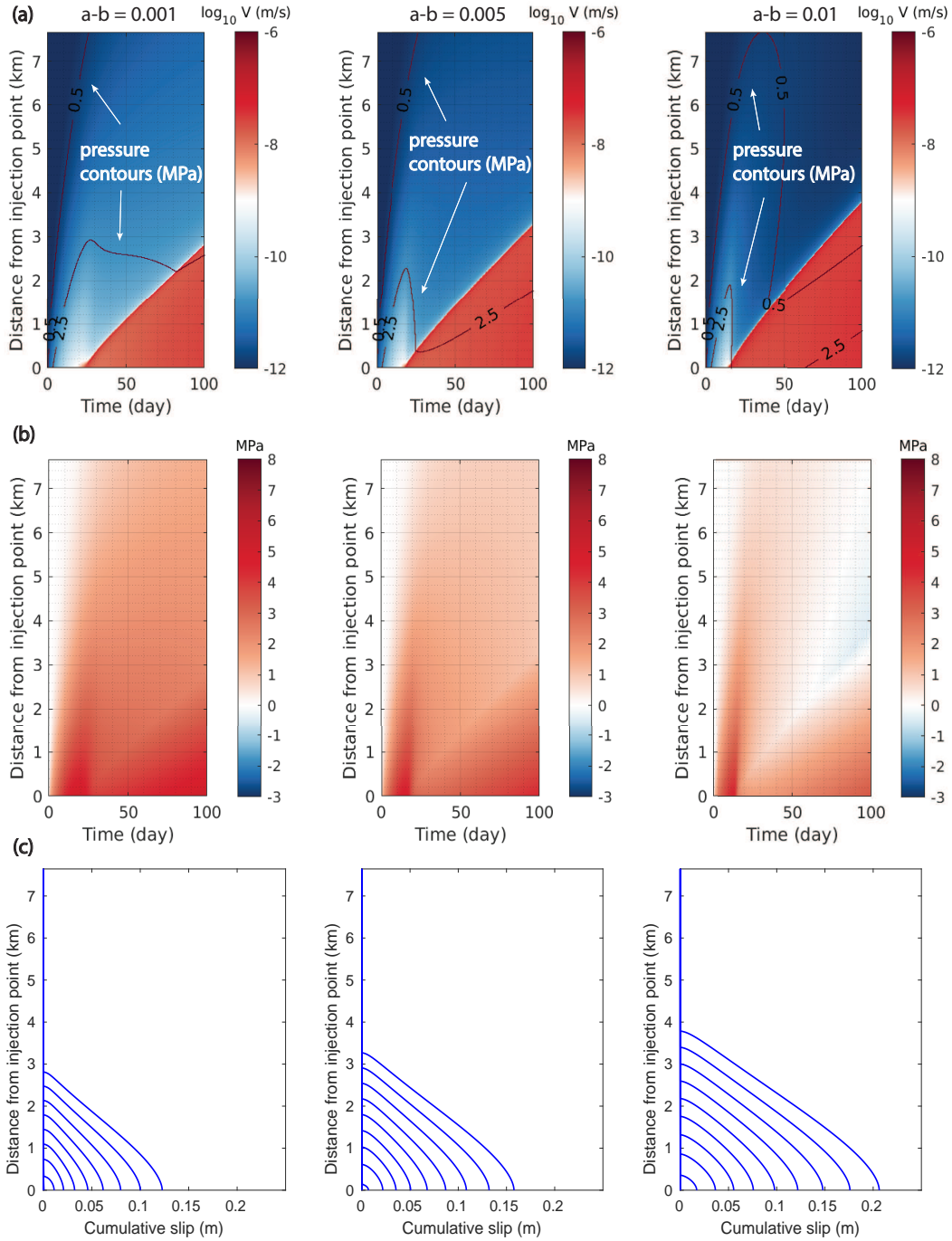


**Figure 11.** Space-time plots of (a) slip velocity and (b) pressure change, and (c) cumulative slip at 10-day intervals, for  $a - b = 0.001, 0.005$  and  $0.01$ , with  $a = 0.01$  held fixed. Overall, changes in  $a - b$  produce only minor differences in the solution.

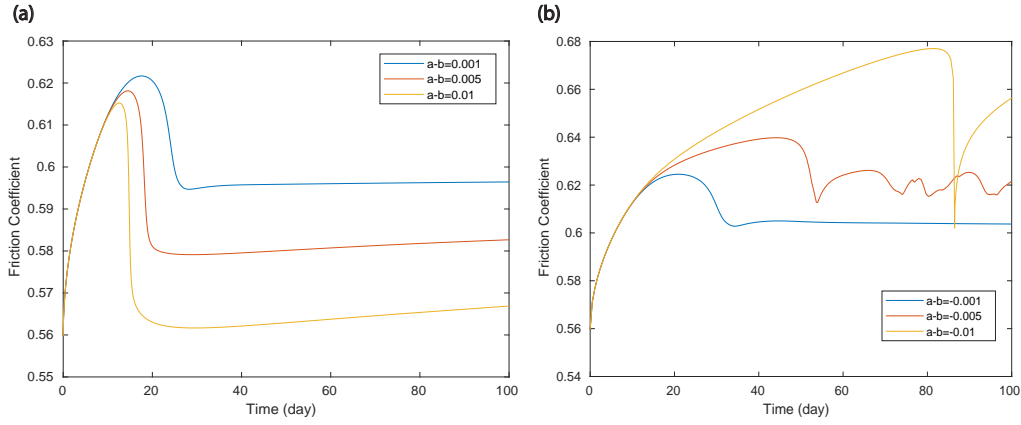


**Figure 12.** Friction coefficient at the injection point for different (a) velocity-strengthening and (b) velocity-weakening properties.

### 3.9 Velocity-weakening Fault

465

466

467

468

469

470

471

Thus far we have examined only velocity-strengthening faults. Here we explore velocity-weakening faults, starting with a reference case that is identical to the reference velocity-strengthening case (Figures 3–5) except with  $a - b = -0.005$ . For velocity-weakening friction, we do not present a comparison for different prestress, initial state variable, or frictional properties, as they show similar trends to the velocity-strengthening case. However, we do study the influence of injection rate.

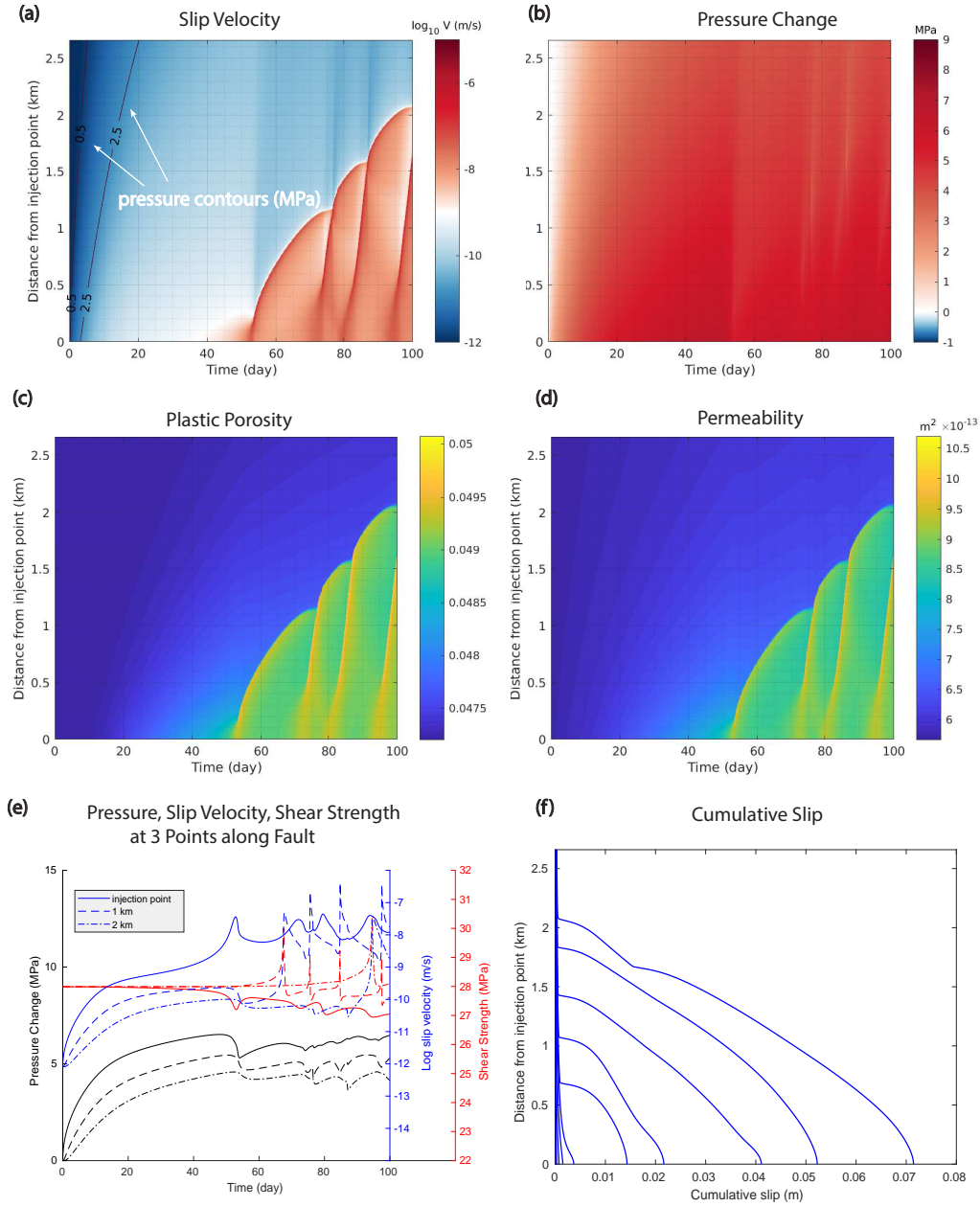


**Figure 13.** Fault response to fluid injection with velocity-weakening friction ( $a - b = -0.005$ ). Space-time plots of (a) Slip velocity, (b) pressure change, (c) plastic porosity, and (d) permeability. (e) Time series of pressure change (black), slip velocity (blue), and shear strength (red) at three points along the fault:  $z = 0, 1$  km, and 2 km. (f) Cumulative slip plotted at 10-day intervals. Velocity-weakening friction leads to spontaneously forming slip pulses instead of a single slip front migrating at constant rate as in the velocity-strengthening case. Triggering of slip is also delayed.

472 The slip behavior for velocity-weakening friction is quite different from the velocity-  
 473 strengthening case. Rather than a single slip front migrating outward at a constant,  
 474 fluid injection drives multiple slip pulses that are spontaneously generated at the in-  
 475 jection site. These slip pulses successively advance on the previously slipped part of the fault,

476 incrementally advancing the overall slip front. Each slip pulse has its own front featur-  
477 ing concentrations in stress and slip velocity (Figure 13a), and behind these fronts the  
478 slip velocity drops by over an order of magnitude. This translates to dilation and per-  
479 meability enhancement at the slip pulse fronts but compaction and healing inside (Fig-  
480 ure 13c-d). Because the maximum slip velocity is about an order of magnitude higher  
481 than in the velocity-strengthening case (compare Figures 3a and 13a), dilatancy is also  
482 more substantial. This is most evident in the pressure time series plots (compare Fig-  
483 ures 5a and 13e).

484 As we increase the injection rate, these slip pulses become more and more closely  
485 spaced in time (Figure 14). At sufficiently high injection rate, the individual slip pulses  
486 merge together, and the overall aseismic slip front migrates at a constant rate as in a velocity-  
487 strengthening fault. We speculate that after the initiation of each slip pulse, the inte-  
488 rior of the slipped region has reached almost steady sliding conditions which are unsta-  
489 ble to pore pressure perturbations, therefore causing the generation of ensuing slip pulses.  
490 As the injection rate increases, such perturbations become large enough so that these  
491 slip pulses are generated faster and eventually become rather indistinguishable. A lin-  
492 ear stability analysis is needed to further quantify this phenomenon.

493 Slip is triggered at around 50 days for the reference velocity-weakening case, far  
494 later than the 20 days triggering time for the velocity-strengthening case (compare Fig-  
495 ures 3a and 13a). This is because the residual friction coefficient is smaller for velocity-  
496 strengthening friction than for velocity-weakening friction, at the low slip velocities oc-  
497 ccurring within the aseismic slip region (compare to results in Section 3.8; see also Fig-  
498 ure 12).

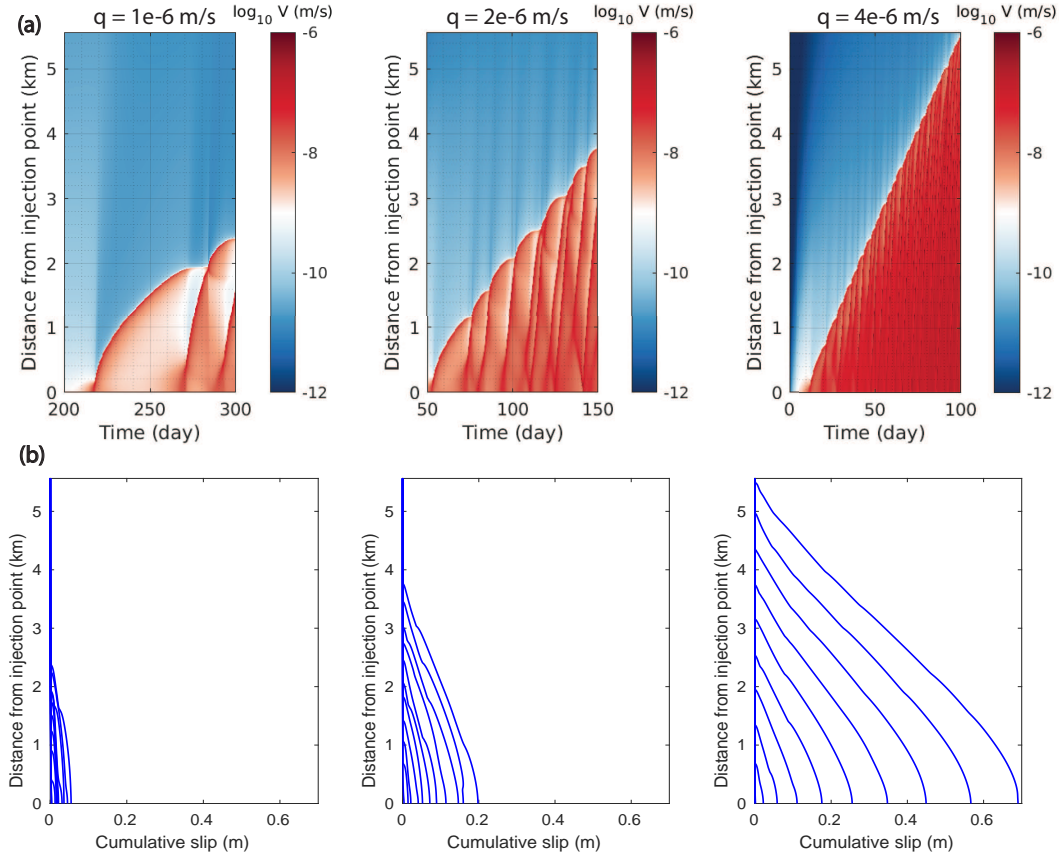


**Figure 14.** (a) Space-time plot of slip velocity for the reference velocity-weakening fault while varying the injection rate. From left to right,  $q_0 = 10^{-6}$ ,  $2 \times 10^{-6}$  and  $4 \times 10^{-6}$  m/s. Shown for 100 days in all cases, but starting when the slip front begins migrating. As injection rate increases, individual slip pulses merge into a single slip front migrating at constant rate. (b) Cumulative slip at 10-day intervals. Total slip is comparable to the velocity-strengthening cases in Figure 9c.

499 Finally, if we neglect porosity and permeability evolution for the reference velocity-  
 500 weakening fault, an earthquake nucleates and ends up rupturing the entire fault (not shown).  
 501 This highlights the importance of the stabilizing effect of dilatancy, which in some cases  
 502 may prevent seismic rupture in response to fluid injection.

## 503 4 Discussion

504 In this section, we first compare our study with previous work involving one-way  
 505 coupling between pore pressure and slip, highlighting the importance of dilatancy. Af-  
 506 ter that, we turn to several observational studies of seismicity triggered by fluid injec-  
 507 tion, comparing the aseismic slip migration rate predicted by our model to observed seis-  
 508 micity patterns. Finally, we discuss some limitations of our model and suggest future im-  
 509 provements.

#### 510 **4.1 Comparison to Models with One-Way Coupling From Pore Pres-** 511 **sure to Slip**

512 Many studies of induced seismicity utilize a one-way coupling from linear pore pres-  
 513 sure diffusion to fault slip (Dieterich et al., 2015; Bhattacharya & Viesca, 2019; Dublan-  
 514 chet, 2019; Laroche et al., 2020), thereby neglecting nonlinearities such as dilatancy. How  
 515 does this impact model predictions? The closest modeling study to ours is by Dublan-  
 516 chet (2019); the 2D model set-up of injection into a fault is identical, except that we use the  
 517 slip law instead of the aging law. We also account for two-way coupling between poros-  
 518 ity, permeability, pore pressure, and slip, whereas Dublan-  
 519 chet (2019) uses a linear pore  
 520 pressure diffusion solution that is one-way coupled to slip. The model of Dublan-  
 521 chet (2019) predicts constant-rate migration of an aseismic slip front when starting from below steady  
 522 state, which he argues is the most probable scenario on real faults. Our model also pre-  
 523 dicts constant-rate aseismic slip front migration, but at a much slower rate. However,  
 524 for a fault initially above steady state, we do not observe an accelerating aseismic slip  
 525 front similar to the nucleation of a dynamic rupture, at least for the range of param-  
 526 eters we explored.

526 The coupling between slip velocity and porosity in our model produces significant  
 527 dilatancy that strengthens the fault and inhibits further destabilization. Dilatancy not  
 528 only changes the slip pattern on the fault, but it also alters the pore pressure diffusion  
 529 pattern, bringing about a more complex relation between the migration speeds of aseis-  
 530 mic slip and pore pressure contours. Various observations might be able to distinguish  
 531 between the linear pore pressure diffusion model and our coupled model, for example,  
 532 measuring pressure and slip in monitoring wells that are hydraulically connected to the  
 533 fault. In comparison, when porosity and permeability evolution are neglected, as in Dublan-  
 534 chet (2019), fault slip begins much sooner, with a higher maximum slip velocity, much faster  
 535 aseismic slip front migration, and a few hundred times more total slip, approaching val-  
 536 ues that seem implausible. For a velocity-weakening fault, the contrast of results is even  
 537 greater. The system transitions from aseismic slip to seismic rupture when the stabiliz-  
 538 ing effects of dilatancy are neglected, whereas we find that dilatancy stabilizes slip and  
 539 leads to complex aseismic slip patterns involving multiple active slip pulses. Overall, these  
 540 results demonstrate that dilatancy can radically change the slip response to injection.

#### 541 **4.2 Connections to Experiments**

542 Our results echo similar conclusions reached by many experimental studies. Lockner  
 543 and Byerlee (1994) demonstrated that dilatancy can suppress shear localization and fa-  
 544 vor distributed shear, likely producing aseismic slip rather than earthquakes. Samuelson  
 545 et al. (2009) noted that shear-induced dilatancy could be of sufficient magnitude to de-  
 546 pressurize pore fluid and inhibit seismic rupture nucleation or propagation. Brantut (2020)  
 547 discussed how the roughness of spontaneously formed faults plays a key role in produc-  
 548 ing strong dilatancy. Results from these studies are generally in agreement with the sta-  
 549 bilizing effect we observe in our simulations. However, dilatancy has not often been em-  
 550 phasized sufficiently in numerical simulations that seek to characterize mechanisms of  
 551 induced seismicity. We believe that this study could serve as a guide for future work that  
 552 integrates essential physical processes to examine injection-induced fault slip. That said,  
 553 there is considerable variability in the experimentally observed porosity and pressure re-  
 554 sponse to slip, with some experiments even showing pressurization from compaction rather  
 555 than suction from dilatancy (Proctor et al., 2020). Future modeling studies should ex-  
 556 plore the compaction limit as well, by changing the sign of the dilatancy parameter  $\epsilon$ .

#### 557 **4.3 Comparison to Observations**

558 Our model makes several predictions that can be used for validation purposes, such  
 559 as the migration rate of the aseismic slip front and slip. Our model predicts slip of a few

centimeters for the lower injection rates we explored, which is consistent with some borehole observations of centimeter-scale aseismic slip in fluid-injection experiments (Cornet et al., 1997; Evans, 2001; Guglielmi et al., 2015). Our model also predicts strains surrounding the fault that might be compared to measurements using fiber optic distributed acoustic sensing (, , ). Additionally, the predicted migration rate of aseismic slip ranges from about 50 to 1000 m/day, depending on the injection rate. There are few direct observations of injection-induced aseismic slip, but many believe that microseismicity, arising from small seismogenic patches within an otherwise aseismically slipping fault, tracks aseismic slip (Dublanche et al., 2013; Jiang & Lapusta, 2016, 2017; Wynants-Morel et al., 2020). This connection is supported by modeling studies employing a heterogeneous mixture of frictional properties, particularly  $a - b$  (Lui & Lapusta, 2016; Luo & Ampuero, 2018; Dublanche et al., 2018; Almakari et al., 2019).

Microseismicity patterns from injection have three general patterns: diffusive, constant rate, and no pattern (Goebel & Brodsky, 2018). Examples of constant-rate migration include the 2003-2004 Corinth Gulf swarm in Greece (Duverger et al., 2015), in which the seismic swarm migrated horizontally over 10 km at an average rate of 50 m/day. Similar patterns were also observed at the Rittershoffen geothermal site in France (Lengliné et al., 2017), where the average migration rate of seismicity was about 300 m/day. Another example is the injection stimulation operation for an enhanced geothermal system project underneath Basel, Switzerland, in 2006. The targeted injection zone consisted of a fractured granite, which showed evidence for preexisting fracture zones and faults with relatively high transmissivity (Goebel & Brodsky, 2018). Injection lasted for 6 days with a total injected volume of 11,570 m<sup>3</sup> (Håring et al., 2008). While the injection rate was gradually increased, the average rate was  $q_0 \approx 2.2 \times 10^{-6}$  m/s, assuming a total area of 10<sup>4</sup> m<sup>2</sup> through which the fluid diffuses (the same as assumed in our model). Using the reference velocity-strengthening case conditions, we predict an aseismic slip migration rate of about 50 m/day for this  $q_0$ . This is remarkably close to the migration rate of about 70 m/day obtained by a linear fit to microseismicity data (Goebel & Brodsky, 2018). A final example is a long-lasting swarm from 2016-2019 near Cahuilla, California, which may have been triggered by the release of a deep, natural fluid source (Ross et al., 2020). The migration speeds of microseismic events are very slow, about 1-5 m/day. This would correspond to an injection rate of about  $1.4 \times 10^{-8}$ - $1.1 \times 10^{-7}$  m/s in our model, by extrapolation of results in Figure 10.

Other earthquake swarms show much faster migration rates, close to 1000 m/day (Shelly et al., 2013, 2016). Such speeds are only sustained for a few days before significant deceleration. Fluid discharge from volcanic sources generally occurs at rather low rates, but it is possible to have intermittent rupturing of permeability seals (Ross et al., 2020) which temporarily results in pulses of high rate flow. This could trigger aseismic slip that migrates at the observed high rates for a short period of time.

#### 4.4 Model Limitations

Arguably the most severe approximation in our study is the neglect of fault-normal fluid flow. Fault-normal flow can reduce or even mitigate dilatancy-induced suction as fluids are drawn in the newly created pore space from the fault zone bordering the slip surface. This process has been examined using a fault-normal pore pressure diffusion model in Segall et al. (2010). The most natural extension of our model would be to account for fluid flow in both the along-fault and fault-normal directions, or even to generalize to full poroelasticity. Based on comparisons between behavior with and without dilatancy, we anticipate that accounting for fault-normal flow will increase the migration rate of aseismic slip fronts as well as the total slip.

In addition, the porosity evolution model we used assumes a positive relation between slip rate and steady state porosity (i.e., shear-induced dilation), but some exper-

611 imental studies provide evidence of shear-enhanced compaction (Tanikawa et al., 2012;  
 612 Faulkner et al., 2018; Proctor et al., 2020). Compaction will pressurize the fault further  
 613 and can even trigger dynamic instability on velocity-strengthening faults (Scuderi et al.,  
 614 2017). Some modeling studies have examined how shear-induced compaction triggered  
 615 by the large stress concentrations ahead of a propagating rupture can rapidly elevate pore  
 616 pressure and weaken the fault surface, promoting rupture propagation (Hirakawa & Ma,  
 617 2016). There is presently little understanding of the conditions that determine whether  
 618 faults will dilate or compact under shear deformation. Some argue that dilatancy would  
 619 be most pronounced for shearing of relatively intact rocks or faults that slip after long  
 620 dormant periods during healing and sealing processes (Brantut, 2020). On the other hand,  
 621 there is also the argument that the comminution effect, and the production of wear prod-  
 622 ucts from fracture surfaces, are mostly dominant during initial shear-in on artificial fresh  
 623 surfaces and for short healing/sealing periods, which may not be broadly representative  
 624 of natural systems (Im et al., 2018). We can conclude from these varied observations that  
 625 porosity evolution with slip is complex and dependent on the initial state of the fault  
 626 zone and how shearing is accommodated within the fault zone. Further experimental work  
 627 is needed to better quantify the relation among porosity, slip, and other relevant mechan-  
 628 ical and hydrological parameters under different faulting conditions.

629 Moreover, the evolution of permeability with porosity is also subject to much vari-  
 630 ability. There could be cases where permeability increases due to pore connectivity en-  
 631 hancement without an actual increase in porosity, as captured through the tortuosity pa-  
 632 rameter in the Kozeny-Carman relation (Bernab et al., 2003). Some recent studies fo-  
 633 cus on this limit, and couple permeability with both effective normal stress and slip while  
 634 neglecting changes in porosity and storage (Zhu et al., 2020). Furthermore, the power-  
 635 law relation between porosity and permeability used in this study also does not have a  
 636 fixed exponent for all processes and rock types (David et al., 1994), nor is it even clear  
 637 if a power-law relation is relevant in all cases. These relations and associated param-  
 638 eters are likely dependent on the specific formation or tectonic history of the region, ar-  
 639 guing for experimental characterization of fluid transport properties from core samples  
 640 when numerical simulations are used for induced seismicity hazard studies. Moreover,  
 641 recent efforts to develop and utilize borehole instrumentation packages to measure pore  
 642 pressure, slip, and other conditions offer the exciting promise of better constraints to val-  
 643 idate models of fluid-induced aseismic slip (Guglielmi et al., 2015; Savage et al., 2017).

644 Finally, some studies also suggest that fault frictional properties evolve during fluid  
 645 injection, thereby influencing the resulting slip. Cappa et al. (2019) showed that faults  
 646 can undergo a transition from velocity weakening to velocity strengthening with increas-  
 647 ing fluid pressure above slip velocities of about 10 mm/s. Scuderi et al. (2017) also ob-  
 648 served that the increase of fluid pressure influences the evolution of the rate-and-state  
 649 friction parameters and consequently the critical nucleation length. Additionally, some  
 650 experiments suggest that pore pressure may alter fault strength in a manner that is more  
 651 complex than just through the Terzaghi effective stress (French et al., 2016). Our model  
 652 has assumed constant rate-and-state parameters for the fault and the standard Terza-  
 653 ghi effective stress model, but in actuality, fluid injection and pressurization may cre-  
 654 ate more complex changes than can be captured through our model framework. Future  
 655 work is needed to better understand effects of pressurization on the frictional strength  
 656 of faults.

## 657 5 Conclusion

658 In this study, we have modeled the aseismic slip resulting from fluid injection in  
 659 a 2D rate-and-state fault coupled with porosity and permeability evolution. Constant  
 660 rate fluid injection into the fault predicts steadily propagating aseismic slip front lags  
 661 behind the linear pressure diffusion prediction of  $z = \sqrt{4\pi ct}$ . However, dilatancy from  
 662 slip alters pore pressure diffusion, such that pore pressure contours migrate at a constant

663 rate that is slower than the aseismic slip front. From our simulation results, we gain the  
 664 following insights:

- 665 1. The evolution of porosity and permeability influences both slip and pore pressure  
 666 diffusion.
- 667 2. Increasing prestress increases the slip velocity and the migration rate of aseismic  
 668 slip. This is because the higher stress drop dominates over a stronger dilatancy  
 669 effect.
- 670 3. Decreasing the initial state variable increases the slip velocity and the migration  
 671 rate of aseismic slip. Dilatancy is approximately the same.
- 672 4. Injection rate, which is the most controllable variable in actual injection opera-  
 673 tions, has a very significant impact on the resulting slip. Lower injection rates de-  
 674 lay the triggering of slip and causes it to migrate at a slower rate. Slip accumu-  
 675 lates at a lower rate, but the total amount of slip is approximately the same when  
 676 the same volume of fluid is injected at different rates. Dilatancy is weaker for lower  
 677 injection rates.
- 678 5. Changing  $a-b$  while keeping  $a$  constant causes only minor differences in the slip  
 679 response. Because slip velocities are less than the reference slip velocity  $V_0$ , the  
 680 overall friction coefficient is lower for more velocity strengthening or less veloc-  
 681 ity weakening faults, which makes the fault slip earlier and at a faster migration  
 682 rate.

683 Overall, we note that nonlinearities in fluid transport, especially dilatancy, funda-  
 684 mentally alter the slip response to injection as compared to slip driven by linear pore  
 685 pressure diffusion. In particular, dilatant strengthening prevents further acceleration of  
 686 the aseismic slip front and, for the parameter choices explored in this study, suppresses  
 687 the onset of seismic slip even in a velocity-weakening fault. In real faults, the evolution  
 688 of porosity and permeability and their impact on fluid pathways, along with the geolog-  
 689 ical structure of the fault and its surrounding damage zone, are much more complex than  
 690 have been explored in this study. However, our simplified formulation is sufficient to demon-  
 691 strate the importance of integrating these hydromechanical processes into numerical mod-  
 692 els, in order to gain a comprehensive understanding of the fluid-rock interaction in injection-  
 693 induced slip.

## 694 Acknowledgments

695 This research was supported by the National Science Foundation (EAR-1947448) and  
 696 the Southern California Earthquake Center (Contribution No. 10846). SCEC is funded  
 697 by NSF Cooperative Agreement EAR-1600087 & USGS Cooperative Agreement G17AC00047.  
 698 We thank Kali Allison and Weiqiang Zhu for assisting with code development. The source  
 699 code is available at <https://bitbucket.org/yyang85/scycle-2>, where a list of input files  
 700 used for this study is also provided. Data used to produce the figures can be found at  
 701 DOI 10.17605/OSF.IO/TV2SX.

## 702 References

- 703 Alghannam, M., & Juanes, R. (2020). Understanding rate effects in injection-  
 704 induced earthquakes. *Nature communications*, *11*(1), 1–6. doi: 10.1038/  
 705 s41467-020-16860-y
- 706 Allison, K. L., & Dunham, E. M. (2018). Earthquake cycle simulations with rate-  
 707 and-state friction and power-law viscoelasticity. *Tectonophysics*, *733*, 232–256.  
 708 doi: 10.1016/j.tecto.2017.10.021
- 709 Almakari, M., Dublanche, P., Chauris, H., & Pellet, F. (2019). Effect of the in-  
 710 jection scenario on the rate and magnitude content of injection-induced seis-  
 711 micity: Case of a heterogeneous fault. *Journal of Geophysical Research: Solid*

- 712 *Earth*, 124(8), 8426–8448. doi: 10.1029/2019JB017898
- 713 Ampuero, J.-P., & Rubin, A. M. (2008). Earthquake nucleation on rate and state  
714 faults—aging and slip laws. *Journal of Geophysical Research: Solid Earth*,  
715 113(B1). doi: 10.1029/2007JB005082
- 716 Andrés, S., Santillán, D., Mosquera, J. C., & Cueto-Felgueroso, L. (2019). Delayed  
717 weakening and reactivation of rate-and-state faults driven by pressure changes  
718 due to fluid injection. *Journal of Geophysical Research: Solid Earth*, 124(11),  
719 11917–11937. doi: 10.1029/2019JB018109
- 720 Bernab, Y., Mok, U., & Evans, B. (2003). Permeability-porosity relationships in  
721 rocks subjected to various evolution processes. *Pure & Applied Geophysics*,  
722 160(5-6), 937-960. doi: 10.1007/PL00012574
- 723 Bhattacharya, P., Rubin, A. M., & Beeler, N. M. (2017). Does fault strengthening  
724 in laboratory rock friction experiments really depend primarily upon time and  
725 not slip? *Journal of Geophysical Research: Solid Earth*, 122(8), 6389–6430.  
726 doi: 10.1002/2017JB013936
- 727 Bhattacharya, P., & Viesca, R. C. (2019). Fluid-induced aseismic fault slip out-  
728 paces pore-fluid migration. *Science*, 364(6439), 464–468. doi: 10.1126/science  
729 .aaw7354
- 730 Brantut, N. (2020). Dilatancy-induced fluid pressure drop during dynamic  
731 rupture: Direct experimental evidence and consequences for earthquake  
732 dynamics. *Earth and Planetary Science Letters*, 538, 116179. doi:  
733 10.1016/j.epsl.2020.116179
- 734 Cappa, F., Guglielmi, Y., Nussbaum, C., & Birkholzer, J. (2018). On the relation-  
735 ship between fault permeability increases, induced stress perturbation, and the  
736 growth of aseismic slip during fluid injection. *Geophysical Research Letters*,  
737 45(20), 11–012. doi: 10.1029/2018GL080233
- 738 Cappa, F., Scuderi, M. M., Collettini, C., Guglielmi, Y., & Avouac, J.-P. (2019).  
739 Stabilization of fault slip by fluid injection in the laboratory and in situ. *Sci-  
740 ence advances*, 5(3), eaau4065. doi: 10.1126/sciadv.aau4065
- 741 Chang, K. W., & Segall, P. (2016). Injection-induced seismicity on basement faults  
742 including poroelastic stressing. *Journal of Geophysical Research: Solid Earth*,  
743 121(4), 2708–2726. doi: 10.1002/2015JB012561
- 744 Civan, F. (2001). Scale effect on porosity and permeability: Kinetics, model, and  
745 correlation. *AIChE journal*, 47(2), 271–287. doi: 10.1002/aic.690470206
- 746 Cornet, F. H., Helm, J., Poitrenaud, H., & Etchecopar, A. (1997). Seismic and aseis-  
747 mic slips induced by large-scale fluid injections. In *Seismicity associated with  
748 mines, reservoirs and fluid injections* (pp. 563–583). doi: 10.1007/978-3-0348  
749 -8814-1\_12
- 750 David, C., Wong, T. F., Zhu, W., & Zhang, J. (1994). Laboratory measurement  
751 of compaction-induced permeability change in porous rocks: Implications for  
752 the generation and maintenance of pore pressure excess in the crust. *Pure &  
753 Applied Geophysics*, 143(1-3), 425-456. doi: 10.1007/BF00874337
- 754 De Barros, L., Cappa, F., Deschamps, A., & Dublanchet, P. (2020). Imbri-  
755 cated aseismic slip and fluid diffusion drive a seismic swarm in the Corinth  
756 Gulf, Greece. *Geophysical Research Letters*, 47(9), e2020GL087142. doi:  
757 10.1029/2020GL087142
- 758 Deng, K., Liu, Y., & Harrington, R. M. (2016). Poroelastic stress triggering of the  
759 December 2013 Crooked Lake, Alberta, induced seismicity sequence. *Geophys-  
760 ical Research Letters*, 43(16), 8482–8491. doi: 10.1002/2016GL070421
- 761 Dieterich, J. H. (1992). Earthquake nucleation on faults with rate-and state-  
762 dependent strength. *Tectonophysics*, 211(1-4), 115–134. doi: 10.1016/  
763 0040-1951(92)90055-B
- 764 Dieterich, J. H., Richards-Dinger, K. B., & Kroll, K. A. (2015). Modeling injection-  
765 induced seismicity with the physics-based earthquake simulator RSQSim. *Seis-  
766 mological Research Letters*, 86(4), 1102–1109. doi: 10.1785/0220150057

- 767 Dublanche, P. (2018, 10). Inferring fault slip rates from cumulative seismic moment  
 768 in a multiple asperity context. *Geophysical Journal International*, *216*(1), 395-  
 769 413. doi: 10.1093/gji/ggy431
- 770 Dublanche, P. (2019). Fluid driven shear cracks on a strengthening rate-and-state  
 771 frictional fault. *Journal of the Mechanics and Physics of Solids*, *132*, 103672.  
 772 doi: 10.1016/j.jmps.2019.07.015
- 773 Dublanche, P., Bernard, P., & Favreau, P. (2013). Interactions and triggering in  
 774 a 3-d rate-and-state asperity model. *Journal of Geophysical Research: Solid  
 775 Earth*, *118*(5), 2225–2245. doi: 10.1002/jgrb.50187
- 776 Duboeuf, L., De Barros, L., Cappa, F., Guglielmi, Y., Deschamps, A., & Seguy, S.  
 777 (2017). Aseismic motions drive a sparse seismicity during fluid injections into a  
 778 fractured zone in a carbonate reservoir. *Journal of Geophysical Research: Solid  
 779 Earth*, *122*(10), 8285–8304. doi: 10.1002/2017JB014535
- 780 Duru, K., Allison, K. L., Rivet, M., & Dunham, E. M. (2019). Dynamic rupture and  
 781 earthquake sequence simulations using the wave equation in second-order form.  
 782 *Geophysical Journal International*, *219*(2), 796–815. doi: 10.1093/gji/ggz319
- 783 Duverger, C., Godano, M., Bernard, P., Lyon-Caen, H., & Lambotte, S. (2015). The  
 784 2003–2004 seismic swarm in the western corinth rift: Evidence for a multiscale  
 785 pore pressure diffusion process along a permeable fault system. *Geophysical  
 786 Research Letters*, *42*(18), 7374–7382. doi: 10.1002/2015GL065298
- 787 Ellsworth, W. L. (2013). Injection-induced earthquakes. *Science*, *341*(6142). doi: 10  
 788 .1126/science.1225942
- 789 Ellsworth, D., Spiers, C. J., & Niemeijer, A. R. (2016). Understanding induced seis-  
 790 micity. *Science*, *354*(6318), 1380–1381. doi: 10.1126/science.aal2584
- 791 Erickson, B. A., & Dunham, E. M. (2014). An efficient numerical method for  
 792 earthquake cycles in heterogeneous media: Alternating subbasin and surface-  
 793 rupturing events on faults crossing a sedimentary basin. *Journal of Geophysical  
 794 Research: Solid Earth*, *119*(4), 3290–3316. doi: 10.1002/2013JB010614
- 795 Evans, K. F. (2001). Determining the effect of stimulation injections on the rock  
 796 mass around the well gpk1 from borehole data: Analysis of the 1993 injections.  
 797 *Data Analysis and Controls Towards Understanding Reservoir Behaviour and  
 798 the Creating of a Conceptual Reservoir Models*, 6–74.
- 799 Evans, K. F., Moriya, H., Niitsuma, H., Jones, R. H., Phillips, W. S., Genter, A., ...  
 800 Baria, R. (2005). Microseismicity and permeability enhancement of hydroge-  
 801 ologic structures during massive fluid injections into granite at 3 km depth at  
 802 the Soultz HDR site. *Geophysical Journal International*, *160*(1), 388–412. doi:  
 803 10.1111/j.1365-246X.2004.02474.x
- 804 Eyre, T. S., Eaton, D. W., Garagash, D. I., Zecevic, M., Venieri, M., Weir, R., &  
 805 Lawton, D. C. (2019). The role of aseismic slip in hydraulic fracturing-induced  
 806 seismicity. *Science advances*, *5*(8), eaav7172. doi: 10.1126/sciadv.aav7172
- 807 Eyre, T. S., Zecevic, M., Salvage, R. O., & Eaton, D. W. (2020). A long-lived swarm  
 808 of hydraulic fracturing-induced seismicity provides evidence for aseismic slip.  
 809 *Bulletin of the Seismological Society of America*. doi: 10.1785/0120200107
- 810 Faulkner, D. R., & Rutter, E. H. (2001). Can the maintenance of overpressured  
 811 fluids in large strike-slip fault zones explain their apparent weakness? *Geology*,  
 812 *29*(6), 503–506. doi: 10.1130/0091-7613(2001)029<0503:CTMOOF>2.0.CO;2
- 813 Faulkner, D. R., Sanchez-Roa, C., Boulton, C., & Den Hartog, S. A. M. (2018). Pore  
 814 fluid pressure development in compacting fault gouge in theory, experiments,  
 815 and nature. *Journal of Geophysical Research: Solid Earth*, *123*(1), 226–241.  
 816 doi: 10.1002/2017JB015130
- 817 French, M. E., Zhu, W., & Banker, J. (2016). Fault slip controlled by stress path  
 818 and fluid pressurization rate. *Geophysical Research Letters*, *43*(9), 4330–4339.  
 819 doi: 10.1002/2016GL068893
- 820 Garagash, D. I., & Germanovich, L. N. (2012). Nucleation and arrest of dynamic  
 821 slip on a pressurized fault. *Journal of Geophysical Research: Solid Earth*,

- 117(B10). doi: 10.1029/2012JB009209
- 822 Goebel, T. H. W., & Brodsky, E. E. (2018). The spatial footprint of injection wells  
823 in a global compilation of induced earthquake sequences. *Science*, *361*(6405),  
824 899–904. doi: 10.1126/science.aat5449
- 825 Goebel, T. H. W., Hosseini, S. M., Cappa, F., Hauksson, E., Ampuero, J. P., Amin-  
826 zadeh, F., & Saleeby, J. B. (2016). Wastewater disposal and earthquake swarm  
827 activity at the southern end of the Central Valley, California. *Geophysical*  
828 *Research Letters*, *43*(3), 1092–1099. doi: 10.1002/2015GL066948
- 829 Goebel, T. H. W., Weingarten, M., Chen, X., Haffener, J., & Brodsky, E. E. (2017).  
830 The 2016 Mw 5.1 Fairview, Oklahoma earthquakes: Evidence for long-range  
831 poroelastic triggering at ~40 km from fluid disposal wells. *Earth and Planetary*  
832 *Science Letters*, *472*, 50–61. doi: 10.1016/j.epsl.2017.05.011
- 833 Guglielmi, Y., Cappa, F., Avouac, J.-P., Henry, P., & Elsworth, D. (2015). Seis-  
834 micity triggered by fluid injection–induced aseismic slip. *Science*, *348*(6240),  
835 1224–1226. doi: 10.1126/science.aab0476
- 836 Handin, J. (1969). On the Coulomb-Mohr failure criterion. *Journal of Geophysical*  
837 *Research*, *74*(22), 5343–5348. doi: 10.1029/JB074i022p05343
- 838 Häring, M. O., Schanz, U., Ladner, F., & Dyer, B. C. (2008). Characterisation of  
839 the basel 1 enhanced geothermal system. *Geothermics*, *37*(5), 469–495. doi: 10  
840 .1016/j.geothermics.2008.06.002
- 841 Heimisson, E. R., Dunham, E. M., & Almquist, M. (2019). Poroelastic effects  
842 destabilize mildly rate-strengthening friction to generate stable slow slip  
843 pulses. *Journal of the Mechanics and Physics of Solids*, *130*, 262–279. doi:  
844 10.1016/j.jmps.2019.06.007
- 845 Hirakawa, E., & Ma, S. (2016). Dynamic fault weakening and strengthen-  
846 ing by gouge compaction and dilatancy in a fluid-saturated fault zone.  
847 *Journal of Geophysical Research: Solid Earth*, *121*(8), 5988–6008. doi:  
848 10.1002/2015JB012509
- 849 Horton, S. (2012). Disposal of hydrofracking waste fluid by injection into subsur-  
850 face aquifers triggers earthquake swarm in central Arkansas with potential for  
851 damaging earthquake. *Seismological Research Letters*, *83*(2), 250–260. doi:  
852 10.1785/gssrl.83.2.250
- 853 Im, K., Elsworth, D., & Fang, Y. (2018). The influence of preslip sealing on the  
854 permeability evolution of fractures and faults. *Geophysical Research Letters*,  
855 *45*(1), 166–175. doi: 10.1002/2017GL076216
- 856 Im, K., Elsworth, D., & Wang, C. (2019). Cyclic permeability evolution during re-  
857 pose then reactivation of fractures and faults. *Journal of Geophysical Research:*  
858 *Solid Earth*, *124*(5), 4492–4506. doi: 10.1029/2019JB017309
- 859 Jiang, J., & Lapusta, N. (2016). Deeper penetration of large earthquakes on seis-  
860 mically quiescent faults. *Science*, *352*(6291), 1293–1297. doi: 10.1126/science  
861 .aaf1496
- 862 Jiang, J., & Lapusta, N. (2017). Connecting depth limits of interseismic lock-  
863 ing, microseismicity, and large earthquakes in models of long-term fault  
864 slip. *Journal of Geophysical Research: Solid Earth*, *122*(8), 6491–6523. doi:  
865 10.1002/2017JB014030
- 866 Johannes, H., Coltman, E., & Class, H. (2018). Porosity-permeability rela-  
867 tions for evolving pore space: A review with a focus on (bio-)geochemically  
868 altered porous media. *Transport in Porous Media*, *124*, 589–629. doi:  
869 10.1007/s11242-018-1086-2
- 870 Keranen, K. M., Savage, H. M., Abers, G. A., & Cochran, E. S. (2013). Potentially  
871 induced earthquakes in Oklahoma, USA: Links between wastewater injection  
872 and the 2011 Mw 5.7 earthquake sequence. *Geology*, *41*(6), 699–702. doi:  
873 10.1126/science.1255802
- 874 Kim, K. H., Ree, J. H., Kim, Y. H., Kim, S. S., Kang, S. Y., & Seo, W. S. (2018).  
875 Assessing whether the 2017 Mw 5.4 Pohang earthquake in South Korea was an

- 877 induced event. *Science*, *360*(6392), 1007–1009. doi: 10.1126/science.aat6081
- 878 Kim, W. Y. (2013). Induced seismicity associated with fluid injection into a deep  
879 well in Youngstown, Ohio. *Journal of Geophysical Research: Solid Earth*,  
880 *118*(7), 3506–3518. doi: 10.1002/jgrb.50247
- 881 Kohli, A. H., & Zoback, M. D. (2013). Frictional properties of shale reservoir rocks.  
882 *Journal of geophysical research: solid earth*, *118*(9), 5109–5125. doi: 10.1002/  
883 jgrb.50346
- 884 Kozydon, J. E., Dunham, E. M., & Nordström, J. (2013). Simulation of dy-  
885 namic earthquake ruptures in complex geometries using high-order finite  
886 difference methods. *Journal of Scientific Computing*, *55*(1), 92–124. doi:  
887 10.1007/s10915-012-9624-5
- 888 Larochelle, S., Lapusta, N., Ampuero, J.-P., & Cappa, F. (2020). *Con-*  
889 *straining fault friction and stability with fluid injection field experiments.*  
890 (<https://www.essoar.org/doi/abs/10.1002/essoar.10504514.1>)
- 891 Lengliné, O., Boubacar, M., & Schmittbuhl, J. (2017). Seismicity related to the hy-  
892 draulic stimulation of grt1, rittershoffen, france. *Geophysical Journal Interna-*  
893 *tional*, *208*(3), 1704–1715. doi: 10.1093/gji/ggw490
- 894 Lockner, D. A., & Byerlee, J. D. (1994). Dilatancy in hydraulically isolated faults  
895 and the suppression of instability. *Geophysical Research Letters*, *21*(22), 2353–  
896 2356. doi: 10.1029/94GL02366
- 897 Lui, S. K. Y., & Lapusta, N. (2016). Repeating microearthquake sequences inter-  
898 act predominantly through postseismic slip. *Nature communications*, *7*(1), 1–  
899 7. doi: 10.1038/ncomms13020
- 900 Luo, Y., & Ampuero, J.-P. (2018). Stability of faults with heterogeneous friction  
901 properties and effective normal stress. *Tectonophysics*, *733*, 257–272. doi: 10  
902 .1016/j.tecto.2017.11.006
- 903 Luquot, L., & Gouze, P. (2009). Experimental determination of porosity and per-  
904 meability changes induced by injection of CO<sub>2</sub> into carbonate rocks. *Chemical*  
905 *Geology*, *265*(1-2), 148–159. doi: 10.1016/j.chemgeo.2009.03.028
- 906 Mase, C. W., & Smith, L. (1987). Effects of frictional heating on the thermal, hy-  
907 drologic, and mechanical response of a fault. *Journal of Geophysical Research:*  
908 *Solid Earth*, *92*(B7), 6249–6272. doi: 10.1029/JB092iB07p06249
- 909 Mazzoldi, A., Rinaldi, A. P., Borgia, A., & Rutqvist, J. (2012). Induced seismicity  
910 within geological carbon sequestration projects: maximum earthquake magni-  
911 tude and leakage potential from undetected faults. *International Journal of*  
912 *Greenhouse Gas Control*, *10*, 434–442. doi: 10.1016/j.ijggc.2012.07.012
- 913 McClure, M. W., & Horne, R. N. (2011). Investigation of injection-induced seismic-  
914 ity using a coupled fluid flow and rate/state friction model. *Geophysics*, *76*(6),  
915 WC181–WC198. doi: 10.1190/GEO2011-0064.1
- 916 McGarr, A., Bekins, B., Burkhardt, N., Dewey, J., Earle, P., Ellsworth, W., . . . Ma-  
917 jer, E. (2015). Coping with earthquakes induced by fluid injection. *Science*,  
918 *347*(6224), 830–831. doi: 10.1126/science.aaa0494
- 919 Menke, H. P., Bijeljic, B., Andrew, M. G., & Blunt, M. J. (2015). Dynamic  
920 three-dimensional pore-scale imaging of reaction in a carbonate at reservoir  
921 conditions. *Environmental science & technology*, *49*(7), 4407–4414. doi:  
922 10.1021/es505789f
- 923 Morrow, C. A., & Byerlee, J. D. (1989). Experimental studies of compaction and  
924 dilatancy during frictional sliding on faults containing gouge. *J. Struct. Geol.*,  
925 *11*(7), 815–825. doi: 10.1016/0191-8141(89)90100-4
- 926 Nelson, P. H. (1994). Permeability-porosity relationships in sedimentary rocks. *The*  
927 *Log Analyst*, *35*(03).
- 928 Norbeck, J. H., & Horne, R. N. (2018). Maximum magnitude of injection-induced  
929 earthquakes: A criterion to assess the influence of pressure migration along  
930 faults. *Tectonophysics*, *733*, 108–118. doi: 10.1016/j.tecto.2018.01.028
- 931 Pampillón, P., Santillán, D., Mosquera, J. C., & Cueto-Felgueroso, L. (2018). Dy-

- 932            namic and quasi-dynamic modeling of injection-induced earthquakes in poroe-  
933            lastic media. *Journal of Geophysical Research: Solid Earth*, 123(7), 5730–5759.  
934            doi: 10.1029/2018JB015533
- 935 Proctor, B., Lockner, D. A., Kilgore, B. D., Mitchell, T. M., & Beeler, N. M. (2020).  
936            Direct evidence for fluid pressure, dilatancy, and compaction affecting slip  
937            in isolated faults. *Geophysical Research Letters*, e2019GL086767. doi:  
938            10.1029/2019GL086767
- 939 Rawling, G. C., Baud, P., & Wong, T. F. (2002). Dilatancy, brittle strength, and  
940            anisotropy of foliated rocks: Experimental deformation and micromechanical  
941            modeling. *Journal of Geophysical Research: Solid Earth*, 107(B10), ETG–8.  
942            doi: 10.1029/2001JB000472
- 943 Rice, J. R. (1992). Fault stress states, pore pressure distributions, and the weakness  
944            of the san andreas fault. In *International geophysics* (Vol. 51, pp. 475–503). El-  
945            sevier.
- 946 Rice, J. R. (1993). Spatio-temporal complexity of slip on a fault. *Journal of Geo-  
947            physical Research: Solid Earth*, 98(B6), 9885–9907. doi: 10.1029/93JB00191
- 948 Rice, J. R. (2006). Heating and weakening of faults during earthquake slip. *Journal  
949            of Geophysical Research: Solid Earth*, 111(B5). doi: 10.1029/2005JB004006
- 950 Rice, J. R., Lapusta, N., & Ranjith, K. (2001). Rate and state dependent  
951            friction and the stability of sliding between elastically deformable solids.  
952            *Journal of the Mechanics and Physics of Solids*, 49(9), 1865–1898. doi:  
953            10.1016/S0022-5096(01)00042-4
- 954 Roland, E., & McGuire, J. J. (2009). Earthquake swarms on transform faults. *Geo-  
955            physical Journal International*, 178(3), 1677–1690. doi: 10.1111/j.1365-246X  
956            .2009.04214.x
- 957 Ross, Z. E., Cochran, E. S., Trugman, D. T., & Smith, J. D. (2020). 3d fault ar-  
958            chitecture controls the dynamism of earthquake swarms. *Science*, 368(6497),  
959            1357–1361. doi: 10.1126/science.abb0779
- 960 Ruina, A. (1983). Slip instability and state variable friction laws. *Jour-  
961            nal of Geophysical Research: Solid Earth*, 88(B12), 10359–10370. doi:  
962            10.1029/JB088iB12p10359
- 963 Saffer, D. M., & Tobin, H. J. (2011). Hydrogeology and mechanics of subduction  
964            zone forearcs: Fluid flow and pore pressure. *Annual Review of Earth and Plan-  
965            etary Sciences*, 39, 157–186. doi: 10.1146/annurev-earth-040610-133408
- 966 Samuelson, J., Elsworth, D., & Marone, C. (2009). Shear-induced dilatancy of fluid-  
967            saturated faults: Experiment and theory. *Journal of Geophysical Research:  
968            Solid Earth*, 114(B12). doi: 10.1029/2008JB006273
- 969 Savage, H. M., Kirkpatrick, J. D., Mori, J. J., Brodsky, E. E., Ellsworth, W. L., Car-  
970            penter, B. M., . . . Kano, Y. (2017). Scientific exploration of induced seismicity  
971            and stress (SEISMS). *Scientific Drilling*, 23. doi: 10.5194/sd-23-57-2017
- 972 Scuderi, M. M., Collettini, C., & Marone, C. (2017). Frictional stability  
973            and earthquake triggering during fluid pressure stimulation of an exper-  
974            imental fault. *Earth and Planetary Science Letters*, 477, 84–96. doi:  
975            10.1016/j.epsl.2017.08.009
- 976 Segall, P., & Lu, S. (2015). Injection-induced seismicity: Poroelastic and earthquake  
977            nucleation effects. *Journal of Geophysical Research: Solid Earth*, 120(7), 5082–  
978            5103. doi: 10.1002/2015JB012060
- 979 Segall, P., & Rice, J. R. (1995). Dilatancy, compaction, and slip instability of a  
980            fluid-infiltrated fault. *Journal of Geophysical Research: Solid Earth*, 100(B11),  
981            22155–22171. doi: 10.1029/95JB02403
- 982 Segall, P., Rubin, A. M., Bradley, A. M., & Rice, J. R. (2010). Dilatant strengthen-  
983            ing as a mechanism for slow slip events. *Journal of Geophysical Research: Solid  
984            Earth*, 115(B12). doi: 10.1029/2010JB007449
- 985 Shapiro, S. A., & Dinske, C. (2009). Scaling of seismicity induced by nonlinear fluid-  
986            rock interaction. *Journal of Geophysical Research: Solid Earth*, 114(B9). doi:

- 987 10.1029/2008JB006145
- 988 Shapiro, S. A., Huenges, E., & Borm, G. (1997). Estimating the crust permeability  
989 from fluid-injection-induced seismic emission at the KTB site. *Geophysical*  
990 *Journal International*, *131*(2), F15–F18. doi: 10.1111/j.1365-246X.1997  
991 .tb01215.x
- 992 Shelly, D. R., Ellsworth, W. L., & Hill, D. P. (2016). Fluid-faulting evolution in  
993 high definition: Connecting fault structure and frequency-magnitude vari-  
994 ations during the 2014 Long Valley Caldera, California, earthquake swarm.  
995 *Journal of Geophysical Research: Solid Earth*, *121*(3), 1776–1795. doi:  
996 10.1002/2015JB012719
- 997 Shelly, D. R., Hill, D. P., Massin, F., Farrell, J., Smith, R. B., & Taira, T. (2013). A  
998 fluid-driven earthquake swarm on the margin of the Yellowstone caldera. *Jour-*  
999 *nal of Geophysical Research: Solid Earth*, *118*(9), 4872–4886. doi: doi:10.1002/  
1000 jgrb.50362
- 1001 Simpson, G., Guéguen, Y., & Schneider, F. (2001). Permeability enhancement  
1002 due to microcrack dilatancy in the damage regime. *Journal of Geophysical*  
1003 *Research: Solid Earth*, *106*(B3), 3999–4016. doi: 10.1029/2000JB900194
- 1004 Szafranski, D., & Duan, B. (2020, 08). Exploring Physical Links between  
1005 Fluid Injection and Nearby Earthquakes: The 2012 Mw 4.8 Timpson,  
1006 Texas, Case Study. *Bulletin of the Seismological Society of America*. doi:  
1007 10.1785/0120200090
- 1008 Tanikawa, W., Mukoyoshi, H., Tadaï, O., Hirose, T., Tsutsumi, A., & Lin, W.  
1009 (2012). Velocity dependence of shear-induced permeability associated with  
1010 frictional behavior in fault zones of the Nankai subduction zone. *Journal of*  
1011 *Geophysical Research: Solid Earth*, *117*(B5). doi: 10.1029/2011JB008956,
- 1012 Torberntsson, K., Stiernström, V., Mattsson, K., & Dunham, E. M. (2018). A fi-  
1013 nite difference method for earthquake sequences in poroelastic solids. *Compu-*  
1014 *tational Geosciences*, *22*(5), 1351–1370. doi: 10.1007/s10596-018-9757-1
- 1015 Viesca, R. C. (2020). *On the existence of a nucleation length for dynamic shear rup-*  
1016 *ture*. (arXiv:submit/3340971)
- 1017 Villiger, L., Gischig, S., Doetsch, J., Krietsch, H., Dutler, O., Jalali, M., . . . others  
1018 (2020). Influence of reservoir geology on seismic response during decameter-  
1019 scale hydraulic stimulations in crystalline rock. *Solid Earth*, *11*(2), 627–655.  
1020 doi: 10.5194/se-11-627-2020
- 1021 Walder, J., & Nur, A. (1984). Porosity reduction and crustal pore pressure devel-  
1022 opment. *Journal of Geophysical Research: Solid Earth*, *89*(B13), 11539–11548.  
1023 doi: 10.1029/JB089iB13p11539
- 1024 Wang, H. F. (2017). *Theory of linear poroelasticity with applications to geomechanics*  
1025 *and hydrogeology*. Princeton: Princeton University Press.
- 1026 Wang, L., Kwiatak, G., Rybacki, E., Bonnelye, A., Bohnhoff, M., & Dresen, G.  
1027 (2020). Laboratory study on fluid-induced fault slip behavior: The role of fluid  
1028 pressurization rate. *Geophysical Research Letters*, *47*(6), e2019GL086627. doi:  
1029 10.1029/2019GL086627
- 1030 Wei, S., Avouac, J.-P., Hudnut, K. W., Donnellan, A., Parker, J. W., Graves, R. W.,  
1031 . . . Cappa, F. (2015). The 2012 Brawley swarm triggered by injection-  
1032 induced aseismic slip. *Earth and Planetary Science Letters*, *422*, 115–125.  
1033 doi: 10.1016/j.epsl.2015.03.054
- 1034 Weingarten, M., Ge, S., Godt, J. W., Bekins, B. A., & Rubinstein, J. L. (2015).  
1035 High-rate injection is associated with the increase in US mid-continent seismic-  
1036 ity. *Science*, *348*(6241), 1336–1340. doi: 10.1126/science.aab1345
- 1037 Wibberley, C. A. J. (2002). Hydraulic diffusivity of fault gouge zones and implica-  
1038 tions for thermal pressurization during seismic slip. *Earth, planets and space*,  
1039 *54*(11), 1153–1171. doi: 10.1186/BF03353317
- 1040 Wiprut, D., & Zoback, M. D. (2000). Fault reactivation and fluid flow along a pre-  
1041 viously dormant normal fault in the northern north sea. *Geology*, *28*(7), 595–

- 1042 598. doi: 10.1130/0091-7613(2000)28<595:FRAFFA>2.0.CO;2
- 1043 Wong, T. F., David, C., & Zhu, W. (1997). The transition from brittle faulting to
- 1044 cataclastic flow in porous sandstones: Mechanical deformation. *Journal of Geo-*
- 1045 *physical Research: Solid Earth*, 102(B2), 3009–3025. doi: 10.1029/96JB03281
- 1046 Wynants-Morel, N., Cappa, F., De Barros, L., & Ampuero, J.-P. (2020). Stress
- 1047 perturbation from aseismic slip drives the seismic front during fluid injection
- 1048 in a permeable fault. *Journal of Geophysical Research: Solid Earth*, 125,
- 1049 e2019JB019179. doi: 10.1029/2019JB019179
- 1050 Yamashita, T. (2013). Generation of slow slip coupled with tremor due to fluid flow
- 1051 along a fault. *Geophysical Journal International*, 193(1), 375–393. doi: 10
- 1052 .1093/gji/ggs117
- 1053 Ye, Z., & Ghassemi, A. (2018). Injection-induced shear slip and permeability en-
- 1054 hancement in granite fractures. *Journal of Geophysical Research: Solid Earth*,
- 1055 123(10), 9009–9032. doi: 10.1029/2018JB016045
- 1056 Yeck, W. L., Hayes, G. P., McNamara, D. E., Rubinstein, J. L., Barnhart, W. D.,
- 1057 Earle, P. S., & Benz, H. M. (2017). Oklahoma experiences largest earth-
- 1058 quake during ongoing regional wastewater injection hazard mitigation efforts.
- 1059 *Geophysical Research Letters*, 44(2), 711–717. doi: 10.1002/2016GL071685
- 1060 Yehya, A., Yang, Z., & Rice, J. R. (2018). Effect of fault architecture and permeabil-
- 1061 ity evolution on response to fluid injection. *Journal of Geophysical Research:*
- 1062 *Solid Earth*, 123(11), 9982–9997. doi: 10.1029/2018JB016550
- 1063 Zhang, L., Soong, Y., Dilmore, R., & Lopano, C. (2015). Numerical simulation
- 1064 of porosity and permeability evolution of Mount Simon sandstone under ge-
- 1065 ological carbon sequestration conditions. *Chemical Geology*, 403, 1–12. doi:
- 1066 10.1016/j.chemgeo.2015.03.014
- 1067 Zhang, Y., Person, M., Rupp, J., Ellett, K., Celia, M. A., Gable, C. W., . . . Mozley,
- 1068 P. (2013). Hydrogeologic controls on induced seismicity in crystalline basement
- 1069 rocks due to fluid injection into basal reservoirs. *Groundwater*, 51(4), 525–538.
- 1070 doi: 10.1111/gwat.12071
- 1071 Zhang, Y., Schaub, P. M., Zhao, C., Ord, A., Hobbs, B. E., & Barnicoat, A. C.
- 1072 (2008). Fault-related dilation, permeability enhancement, fluid flow and min-
- 1073 eral precipitation patterns: numerical models. *Geological Society, London,*
- 1074 *Special Publications*, 299(1), 239–255. doi: 10.1144/SP299.15
- 1075 Zhu, W., Allison, K. L., Dunham, E. M., & Yang, Y. (2020). Fault valving and pore
- 1076 pressure evolution in simulations of earthquake sequences and aseismic slip.
- 1077 *Nature Communications*, 11(4833). doi: 10.1038/s41467-020-18598-z
- 1078 Zhu, W., David, C., & Wong, T. F. (1995). Network modeling of permeability evolu-
- 1079 tion during cementation and hot isostatic pressing. *Journal of Geophysical Re-*
- 1080 *search: Solid Earth*, 100(B8), 15451–15464. doi: 10.1029/95JB00958
- 1081 Zhu, W., & Wong, T. F. (1999). Network modeling of the evolution of permeability
- 1082 and dilatancy in compact rock. *Journal of Geophysical Research: Solid Earth*,
- 1083 104(B2), 2963–2971. doi: 10.1029/1998JB900062
- 1084 Zoback, M. D., Kohli, A., Das, I., & McClure, M. W. (2012). The importance of
- 1085 slow slip on faults during hydraulic fracturing stimulation of shale gas reser-
- 1086 voirs. In *SPE Americas Unconventional Resources Conference*.

Figure 1.

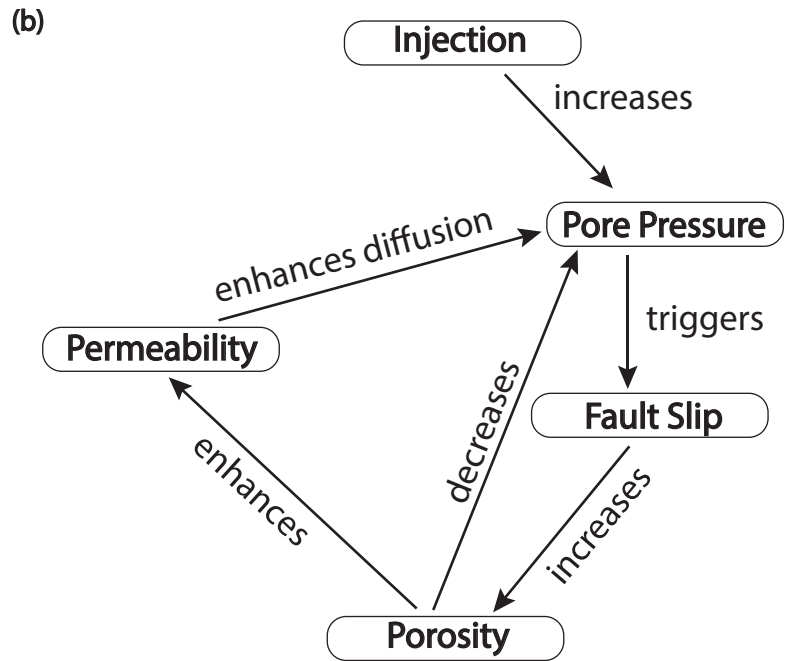
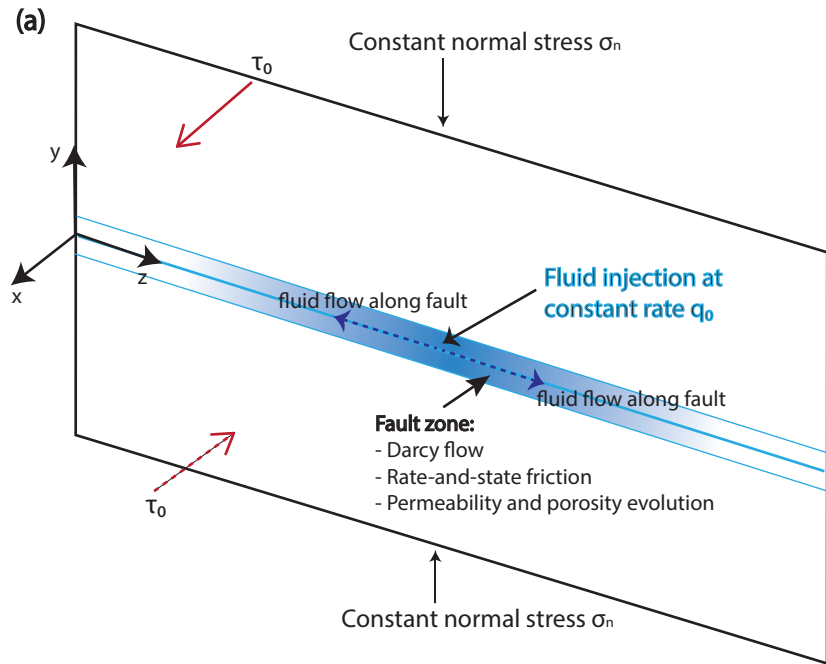


Figure 2.

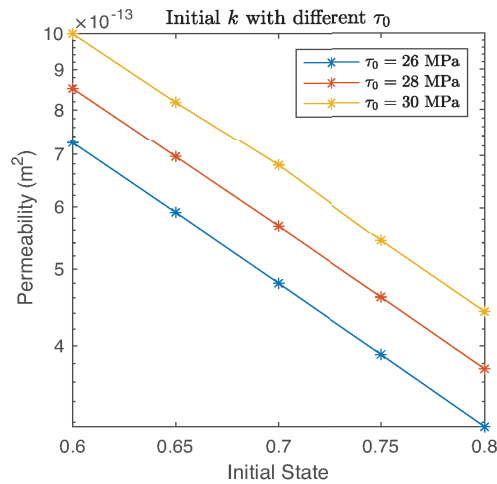
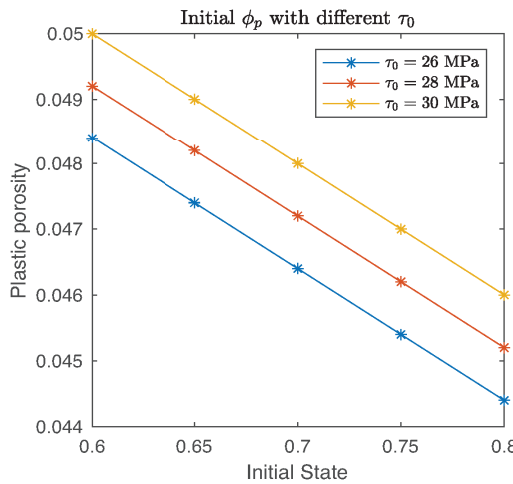
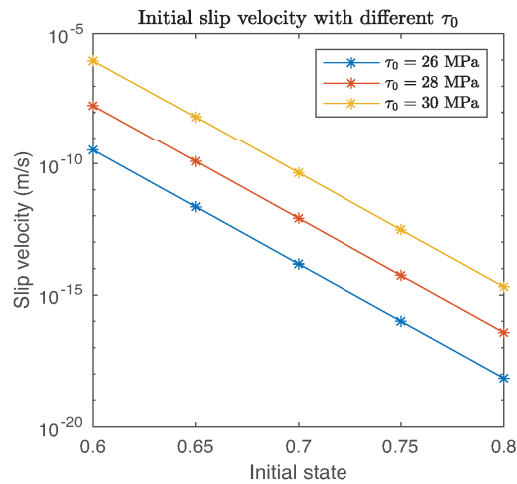
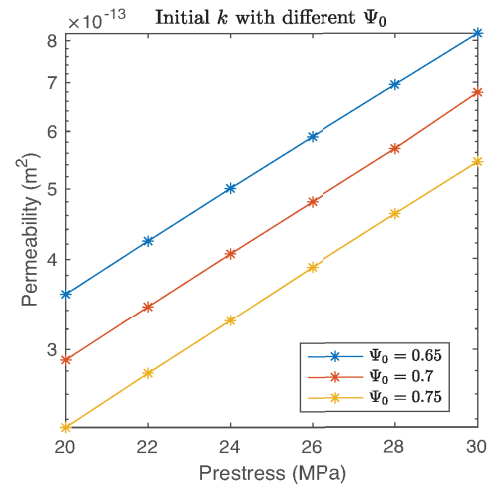
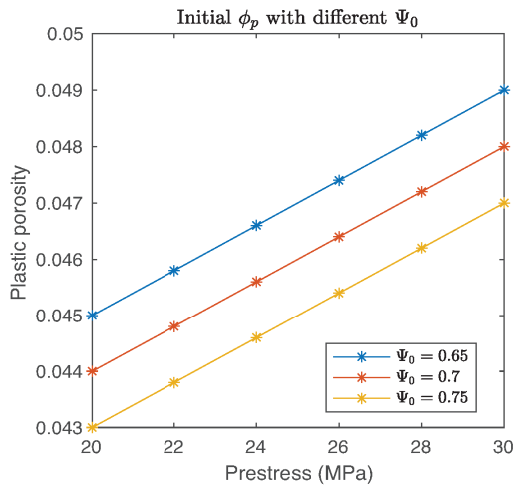
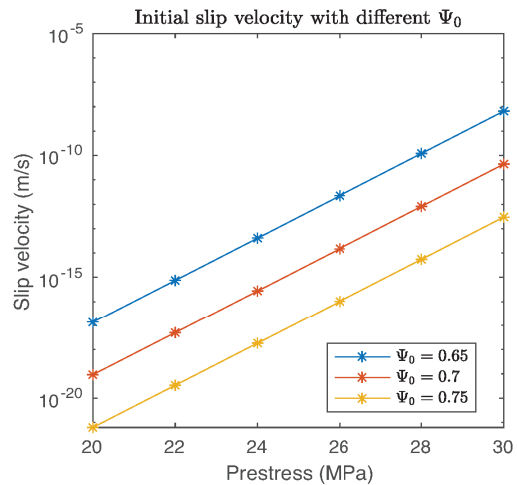


Figure 3.

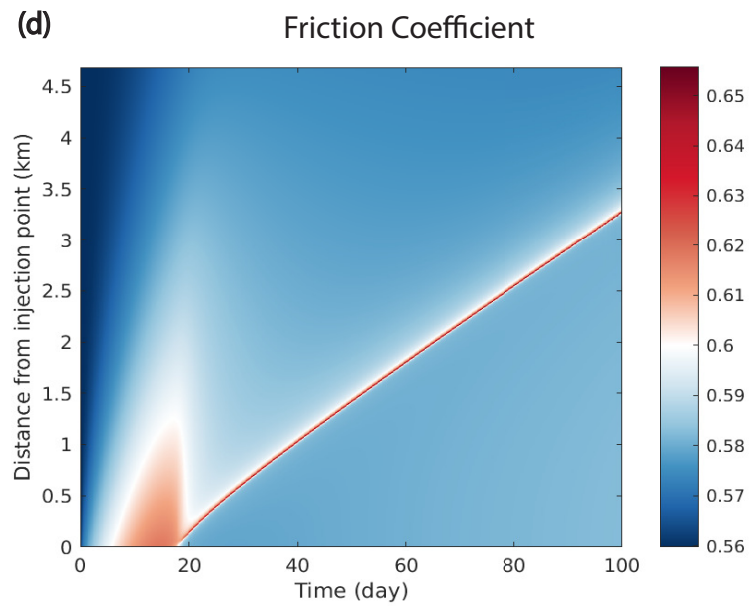
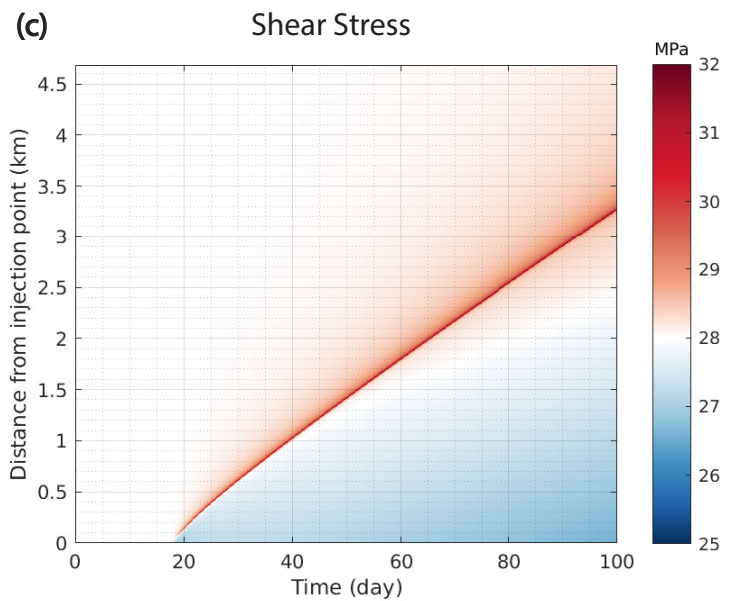
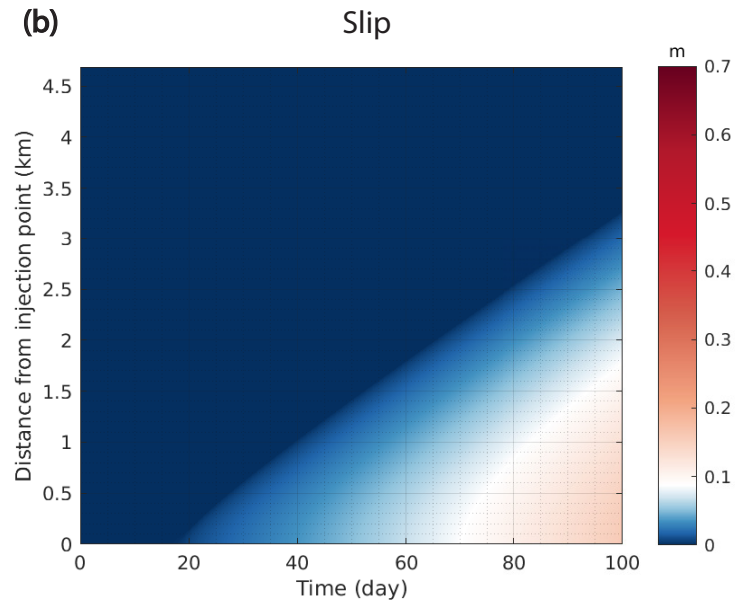
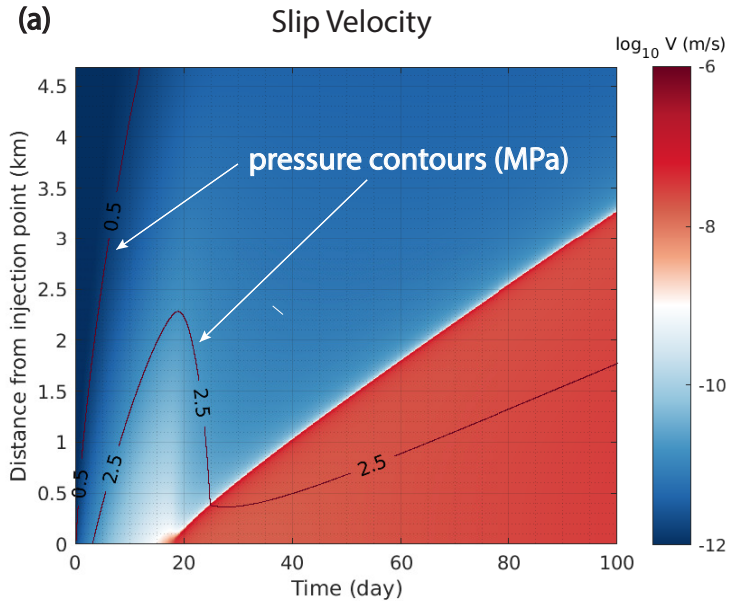


Figure 4.

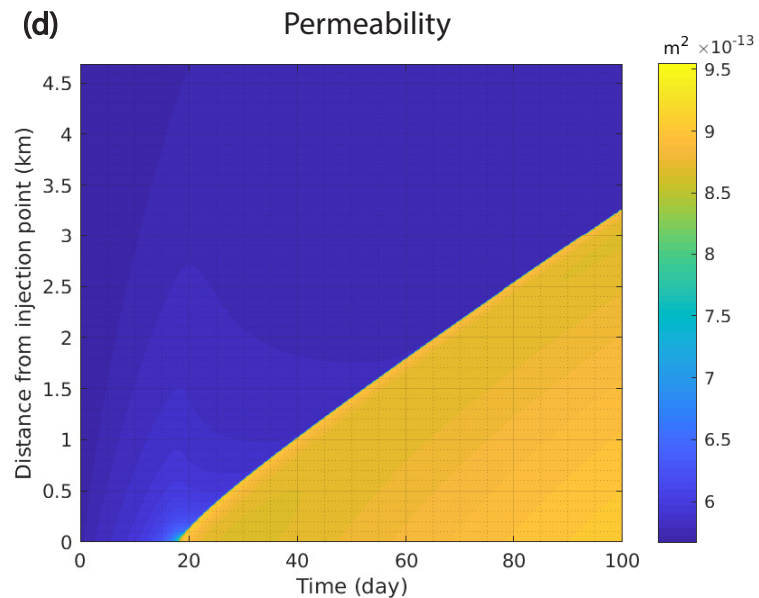
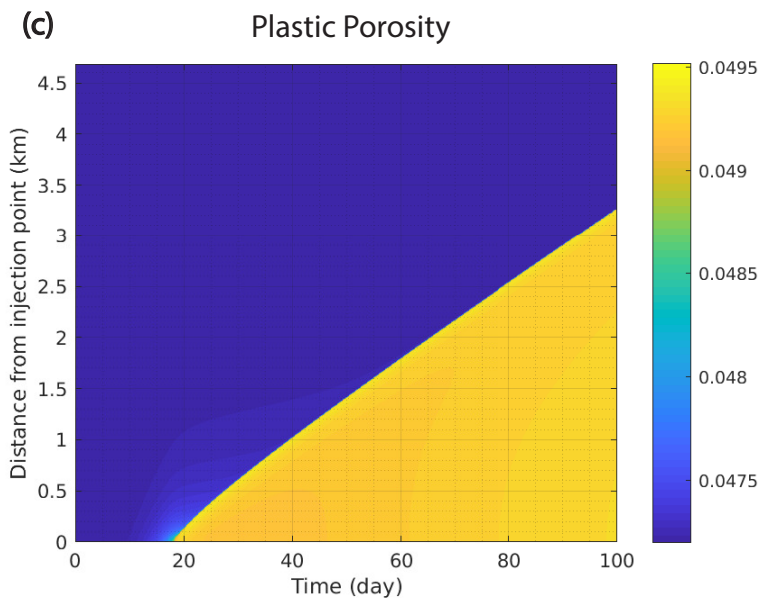
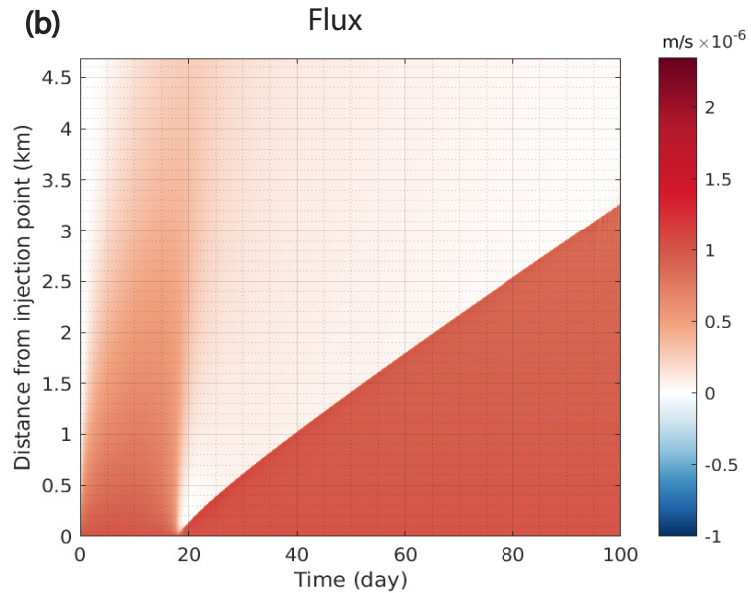
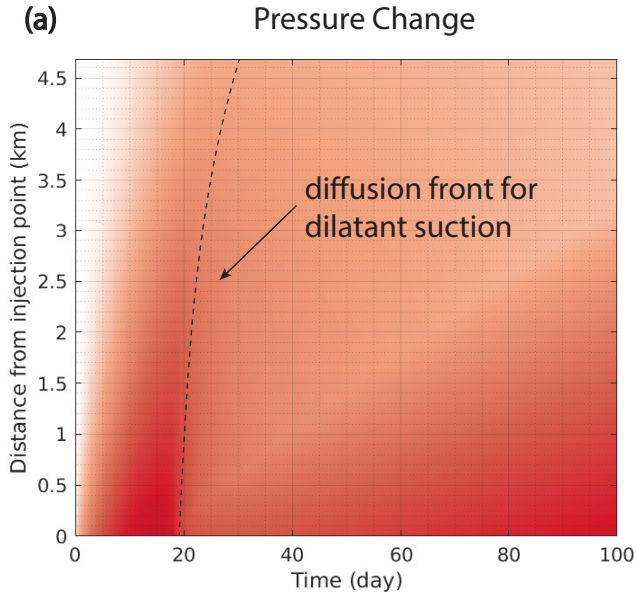
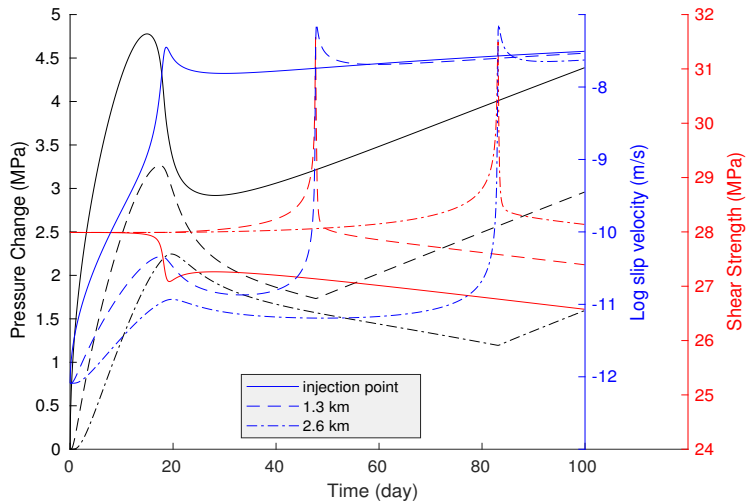


Figure 5.

**(a)** Pressure, Slip Velocity, Shear Strength at 3 Points along Fault



**(b)** Cumulative Slip

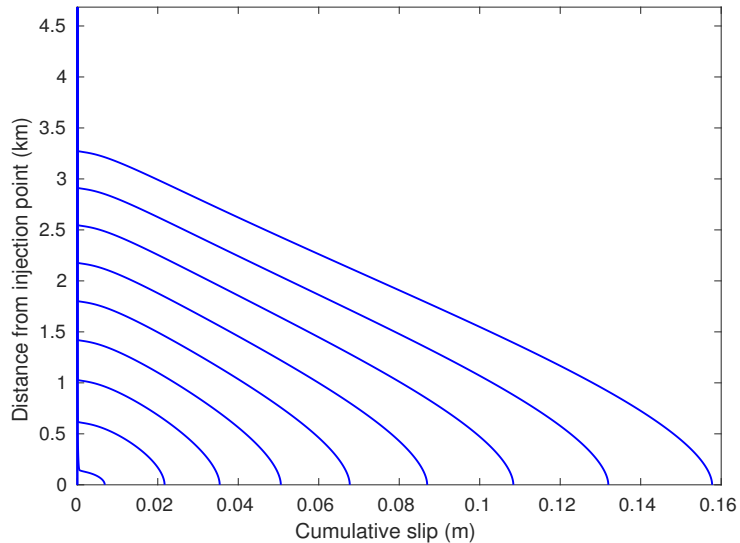


Figure 6.

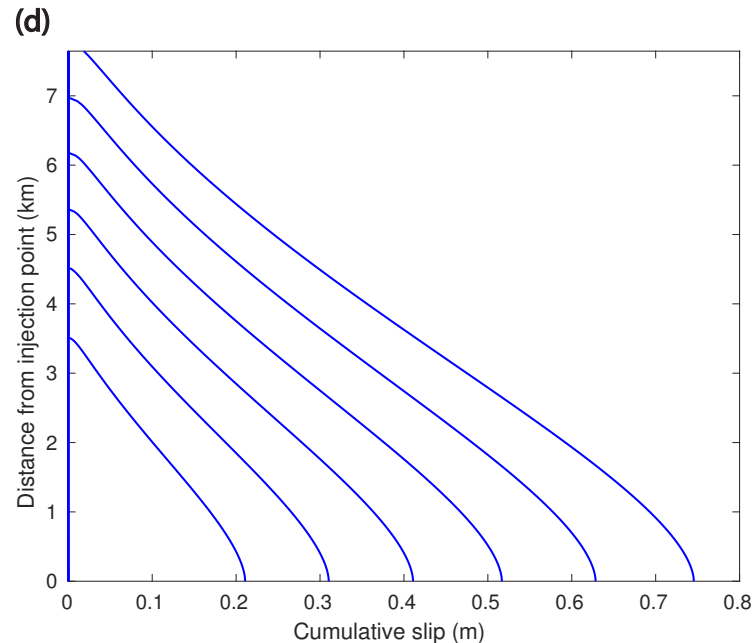
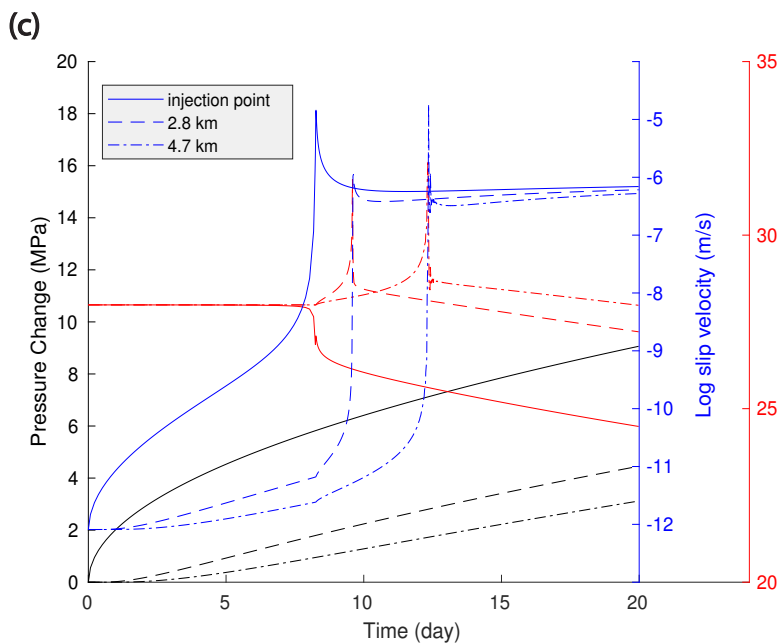
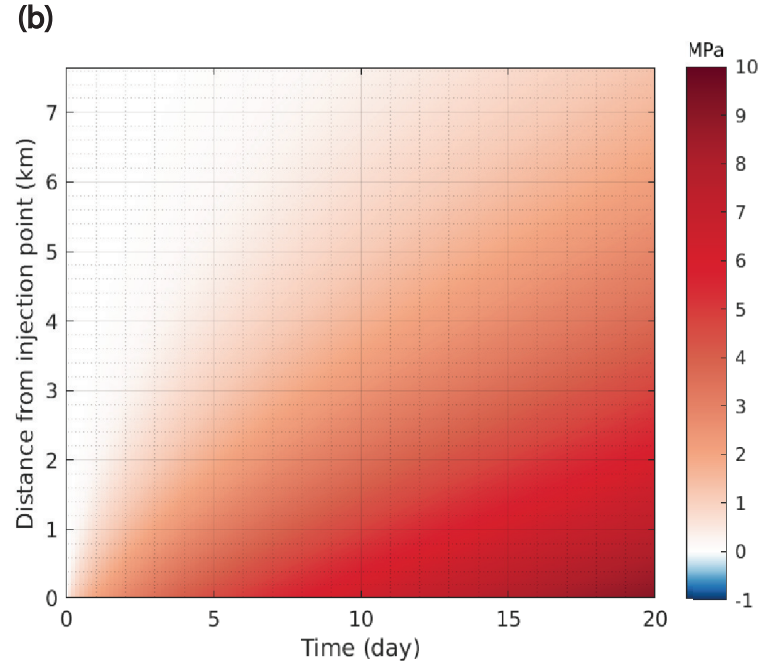
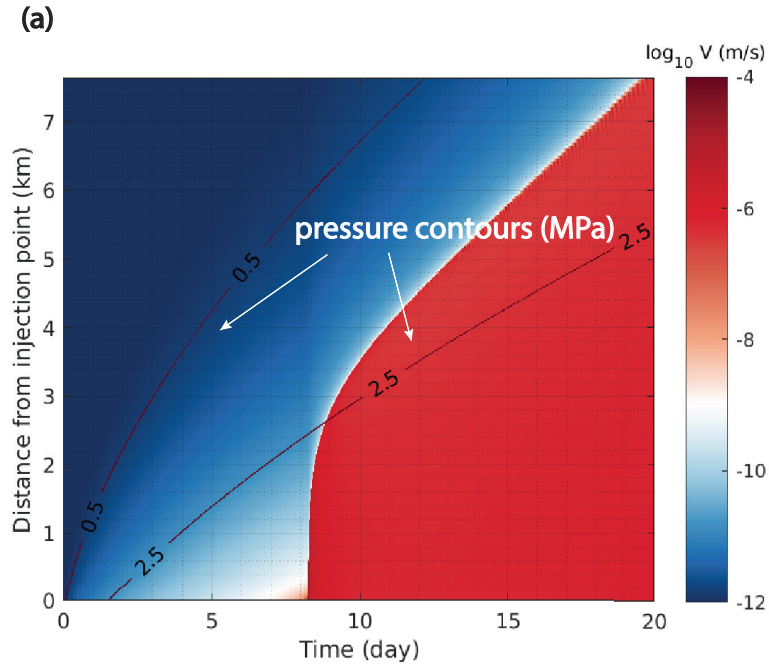


Figure 7.

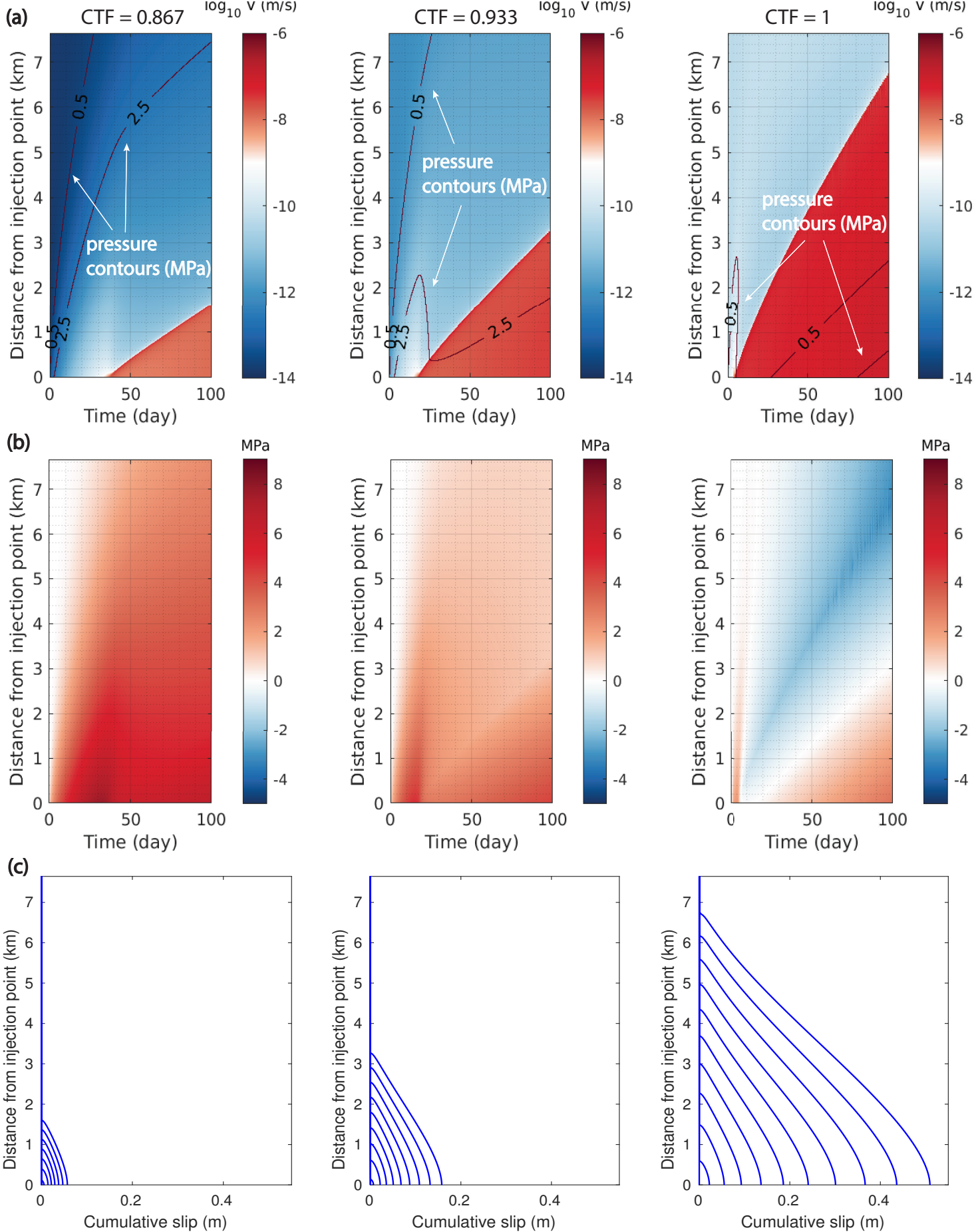


Figure 8.

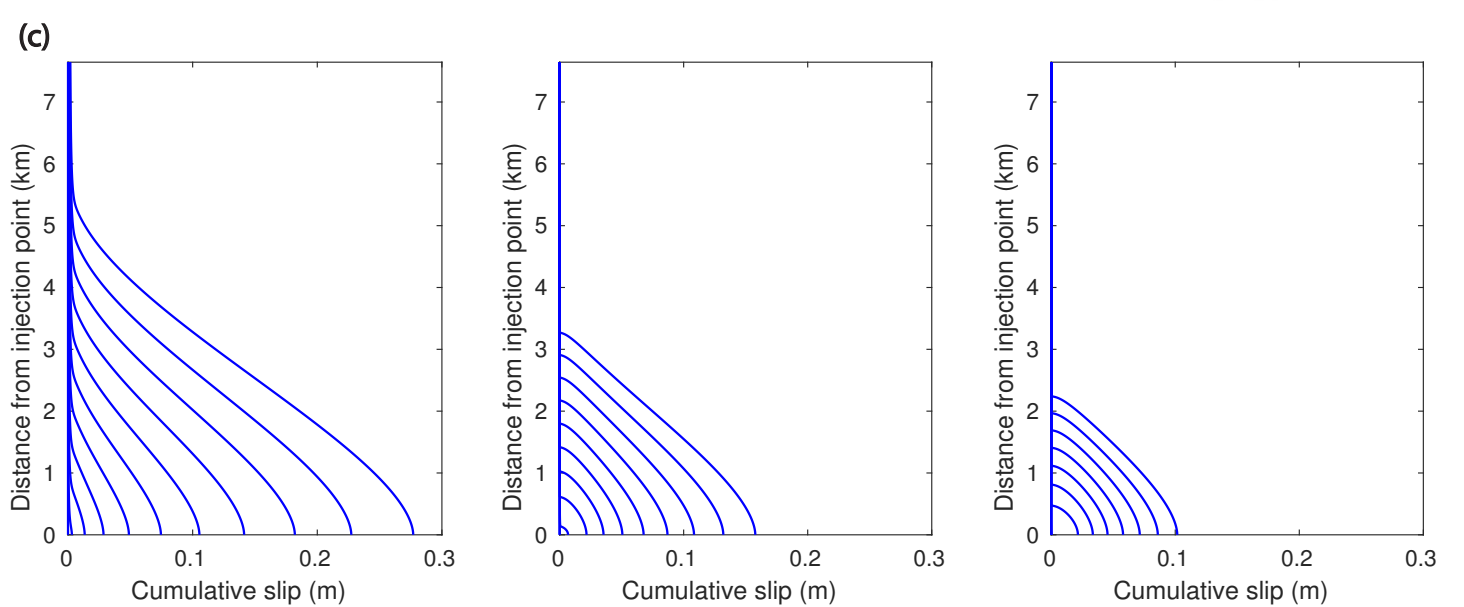
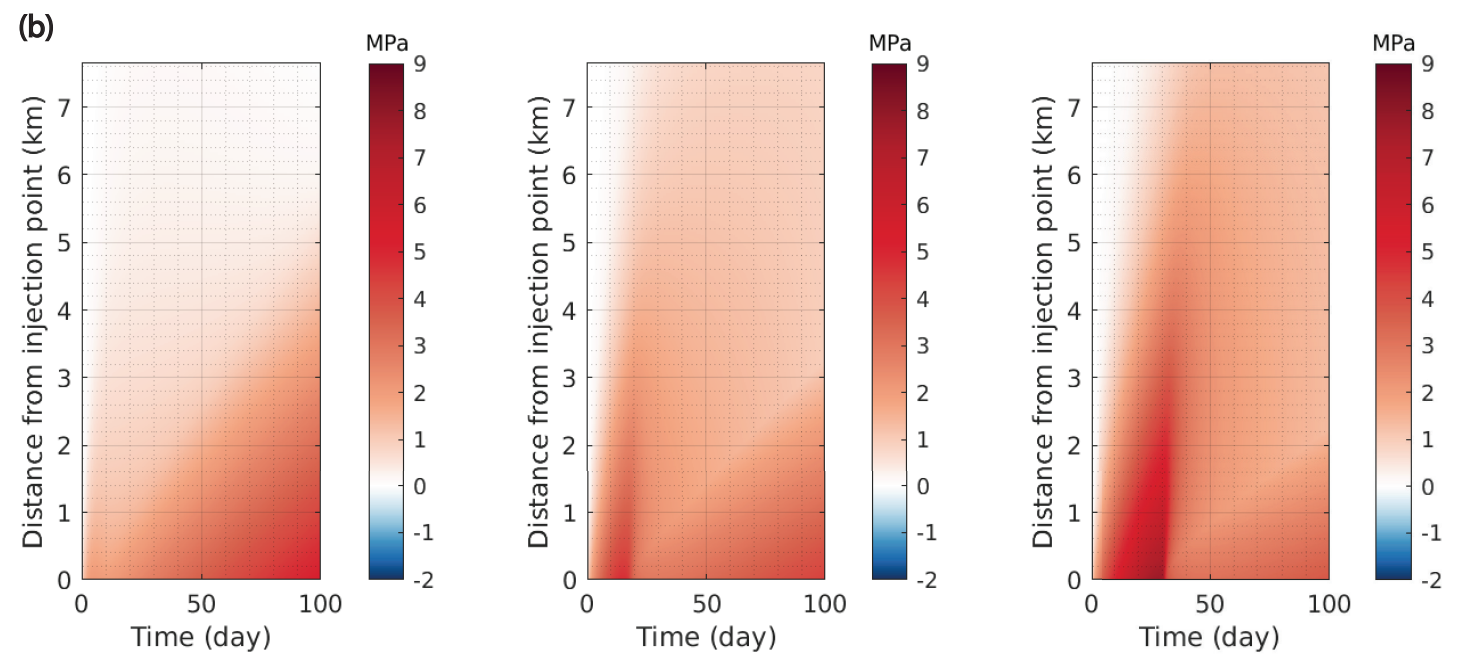
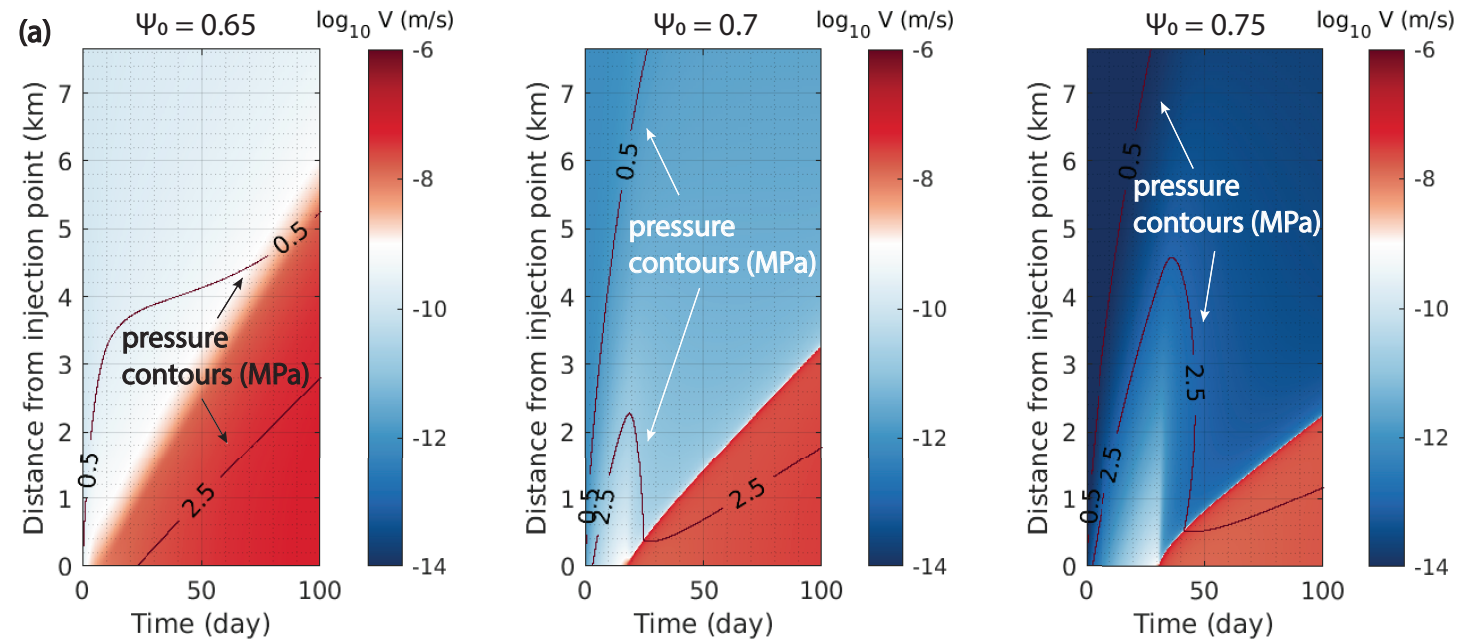


Figure 9.

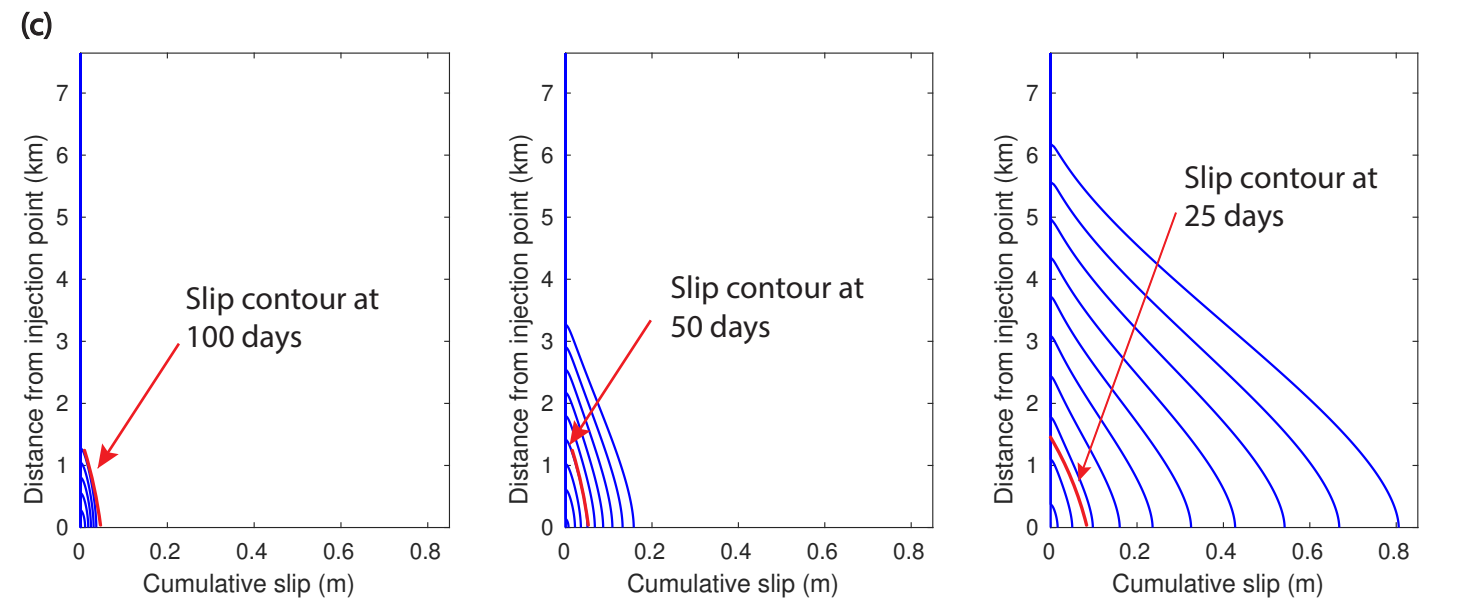
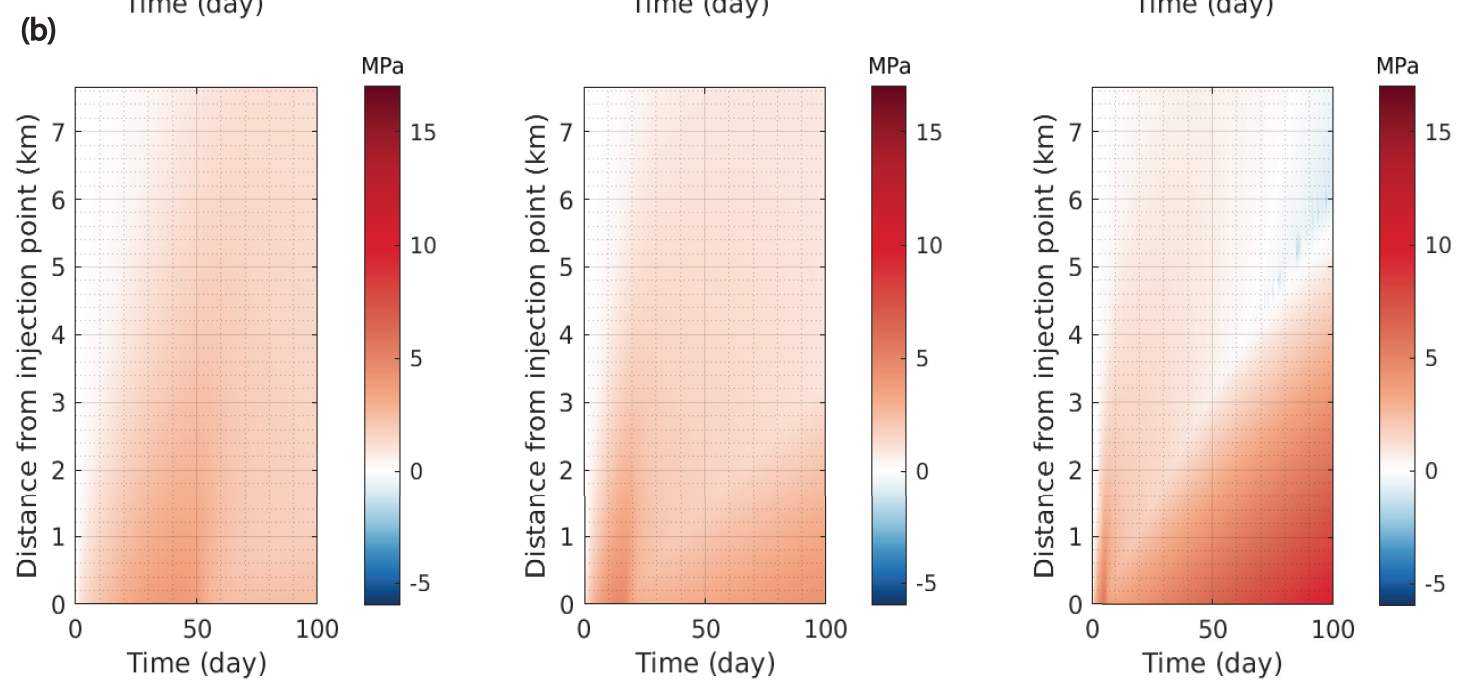
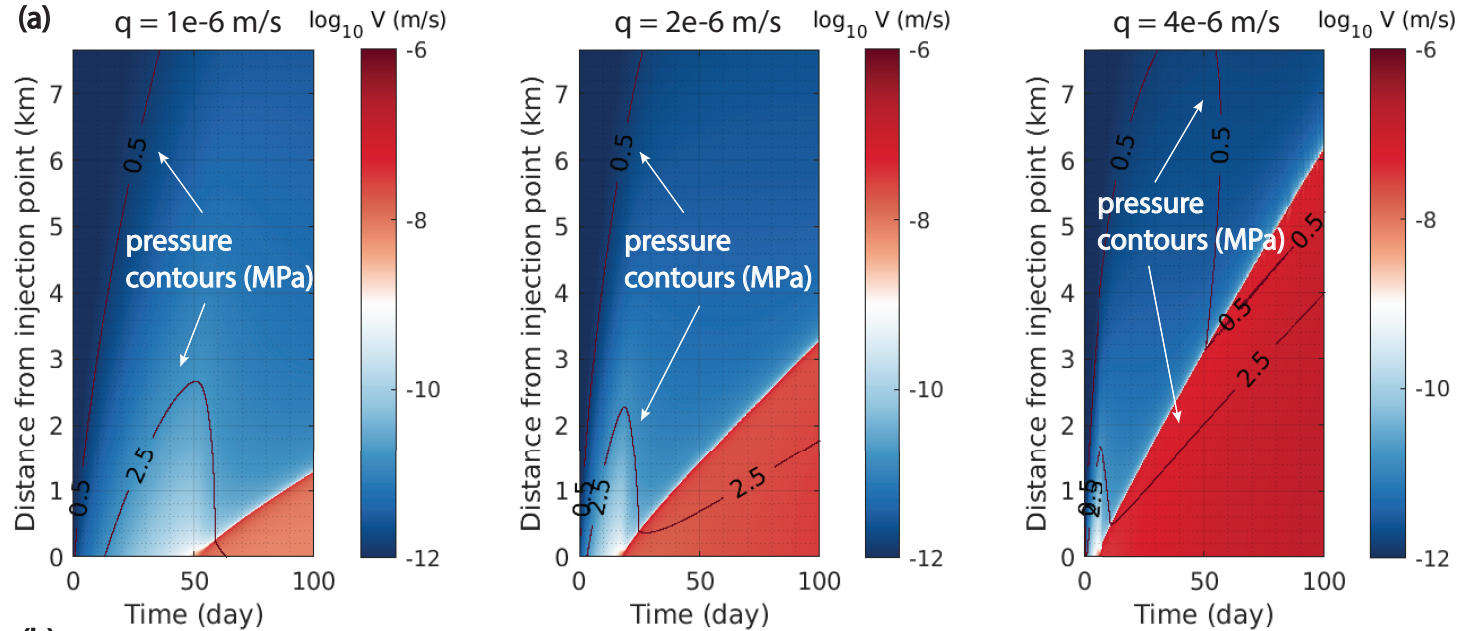


Figure 10.

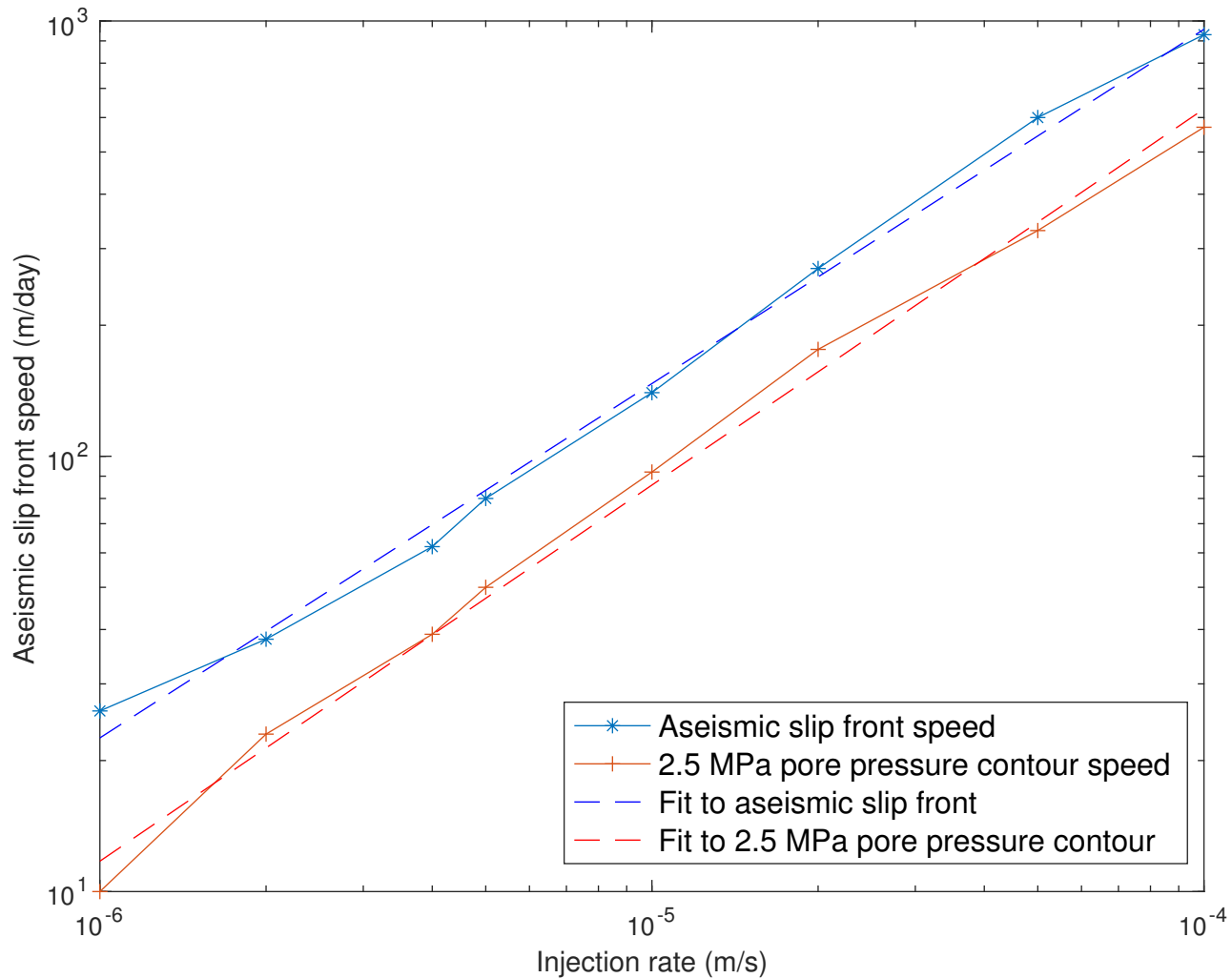


Figure 11.



Figure 12.

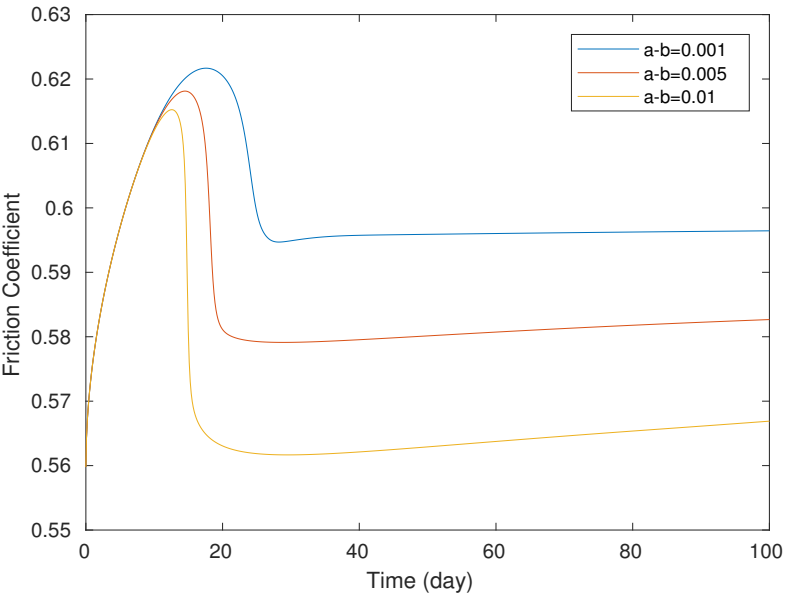
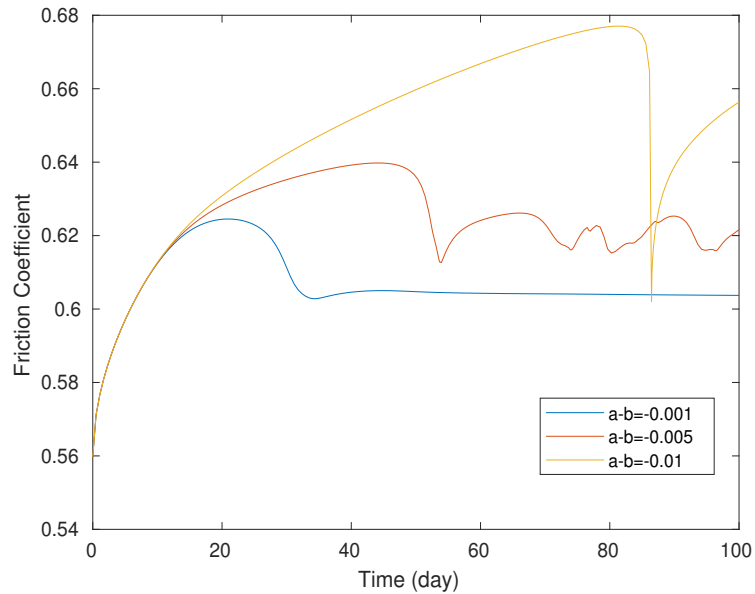
**(a)****(b)**

Figure 13.

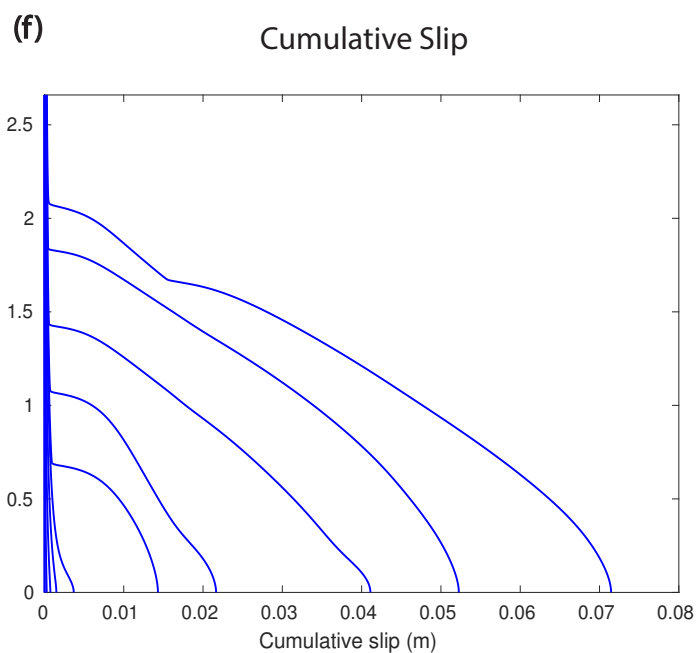
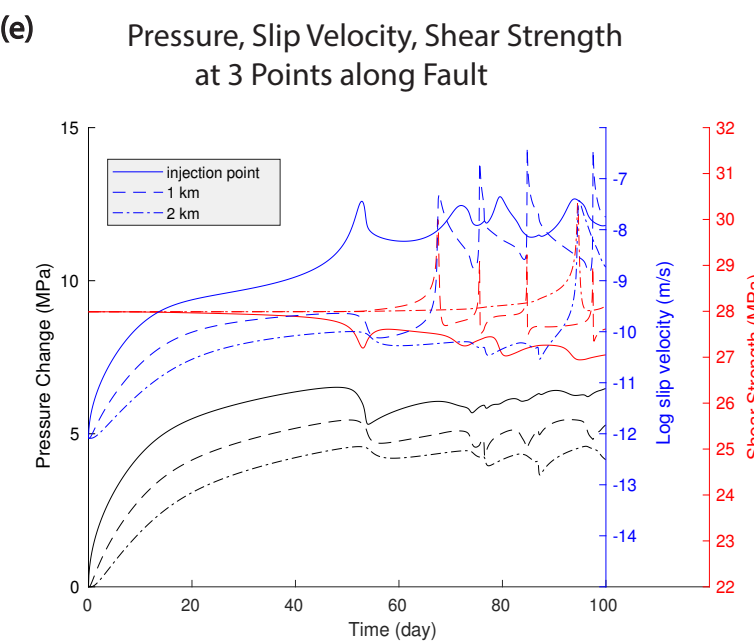
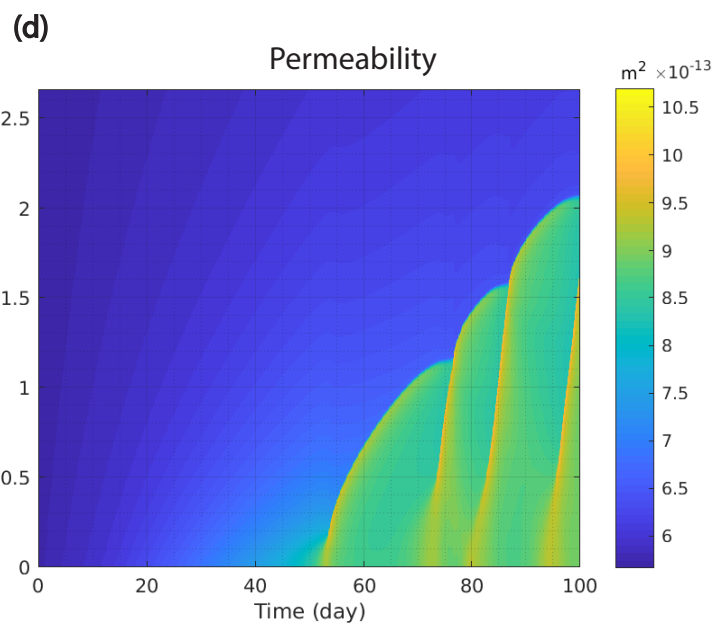
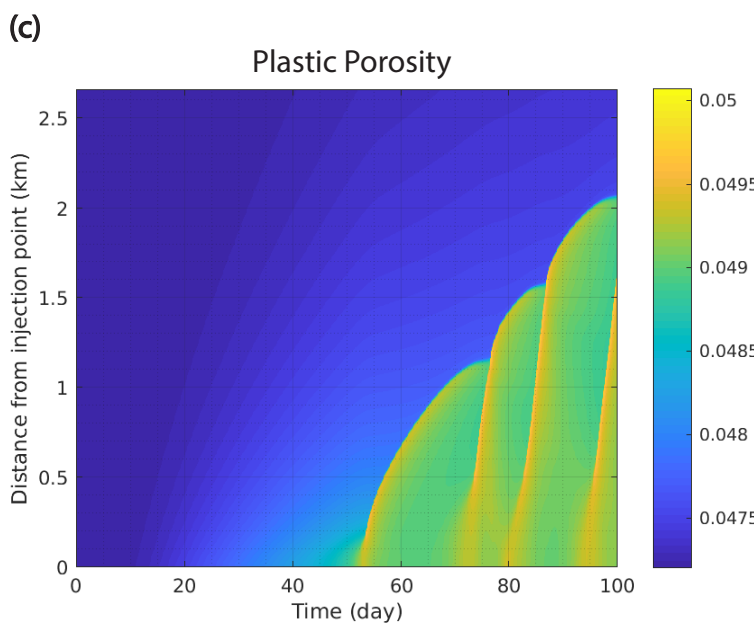
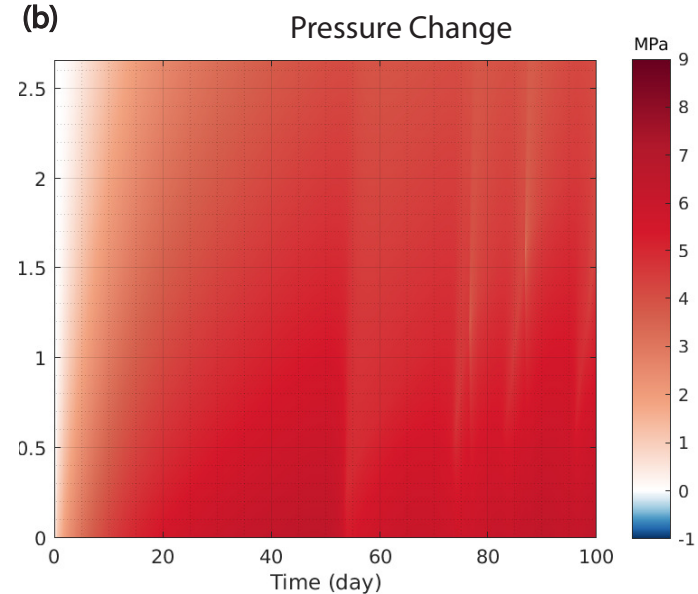
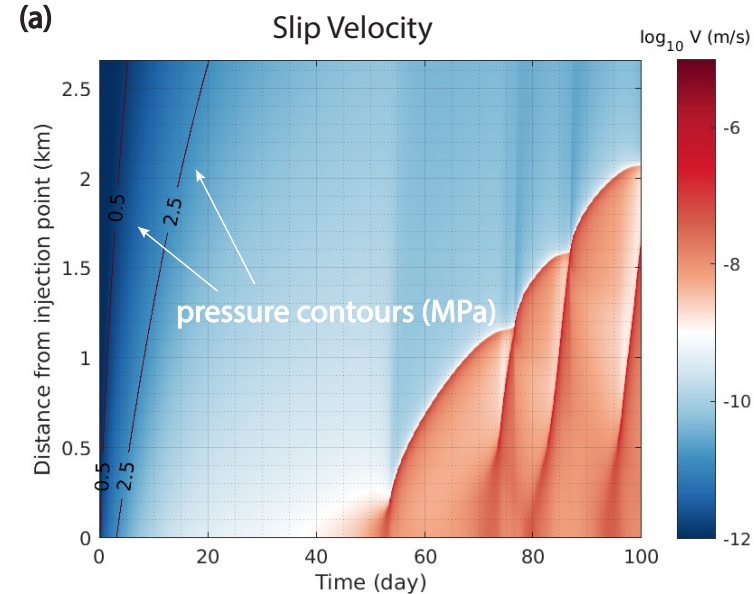


Figure 14.

